The evolution of intraplate fault systems in central Turkey: Structural evidence and Ar-Ar and Rb-Sr age constraints for the Savcili Fault Zone

Veysel Isik[1], I. Tonguç Uysal[2,3], Ayse Caglayan[1], and Gurol Seyitoglu[1]

[1]Department of Geological Engineering, Tectonics Research Group, Ankara University, Ankara, Turkey, [2]Queensland Geothermal Energy Centre of Excellence, University of Queensland, Brisbane, Queensland, Australia, [3]Department of Geological Engineering, Hacettepe University, Beytepe, Ankara, Turkey

Abstract The Savcili Fault Zone represents one of the most prominent regional-scale intraplate fault systems in central Turkey, recording the collisional events following the closure of Neo-Tethys in the eastern Mediterranean region. It consists of anastomosing reverse/thrust faults with WNW-ESE direction that placed rocks of the Central Anatolian Crystalline Complex on Paleogene sedimentary units. Structural measurements and kinematic indicators show that faults within the Savcili Fault Zone (SFZ) have top to the NE and NW sense of brittle deformation. Stable isotope (δ^{18}O and δ D) and trace element data indicate that fault gouge illites precipitated from deep basinal brines. These fluids were mobilized during phases of compressional deformation and migrated upward along thrust faults toward shallow brittle deformation zones. Rb-Sr and Ar-Ar geochronology of fault gouges in two cataclastic zones demonstrates age variability for two different dating techniques (Rb-Sr: 40.9 ± 1.5 Ma and 22.9 ± 1.3 Ma; Ar-Ar: 46.45 ± 0.25 Ma and 29.8 ± 0.13 Ma). We argue that Rb-Sr dating provides ages more closely reflecting the timing of fault movements because of potential contamination of illite by excess ^{40}Ar. Accordingly, the SFZ was active during at least two phases; the middle Eocene and late Oligocene to early Miocene, which is consistent with the relative age constraints suggested by field relationships. Geochronology combined with structural field evidence indicates a rapid change in stress regime from extension to contraction at ~40 Ma that continued until at least ~23 Ma. Direct dating of brittle faulting provides a prolific approach for determining the absolute timing of tectonic events in areas that have largely relied on indirect information.

1. Introduction

The eastern Mediterranean region provides a great opportunity to study the evolution of the Tethyan orogenic belt. Turkey is the most conspicuous part in this region, representing one of the most tectonically active and mobile regions on Earth as a result of the convergent movement of the Eurasian and the African/Arabian plates and progressive closure of the Neo-Tethys during the Late Mesozoic-Cenozoic time [e.g., *Sengor and Yılmaz*, 1981; *Robertson and Dixon*, 1984]. This time signifies the major collisional and extensional events in the eastern Mediterranean region, leading to major imbrications, thrusts at the boundaries of continental blocks, high-grade metamorphism, magmatism, exhumation, and detachment faulting.

The postcollisional tectonics resulted in the formation of a number of regionally important intracontinental fault systems such as Tuzgolu Fault Zone (TFZ), Central Anatolian Fault Zone (CAFZ), and Savcili Fault Zone (SFZ) (Figures 1 and 2). The origin and displacement history of these fault systems has remained highly controversial, mainly because there is a lack of quantitative data. Therefore, kinematic and particularly any quantitative data on the formation mechanism of these intraplate fault systems in central Turkey is crucial for the complex tectonic evolution of the eastern Mediterranean region. TFZ is a NE-SE striking 200 km long and 5 to 25 km wide fault zone [*Dirik and Goncuoglu*, 1996]. A Cretaceous or Miocene age has been suggested for the TFZ, while its kinematic (e.g., right-handed strike-slip fault, normal right-slip fault, reverse right-slip fault) is debatable [e.g., *Gorur et al.*, 1984; *Sengor et al.*, 1985; *Dirik and Goncuoglu*, 1996; *Cemen et al.*, 1999; *Isik*, 2009]. The CAFZ occurs further east in central Turkey. It is striking NE-SW, about 730 km long and 2 to 80 km wide [*Kocyigit and Beyhan*, 1998]. According to *Kocyigit and Beyhan* [1998], CAFZ represents only the certain part of this fault zone that was active during Plio-Quaternary as a sinistral strike-slip movement with a displacement of 24 km. The pre-Pliocene evolution of this fault zone is known as Ecemis Fault Zone (EFZ) representing a 75 km displacement. However, its age is highly controversial [e.g., *Kocyigit and Beyhan*, 1998].
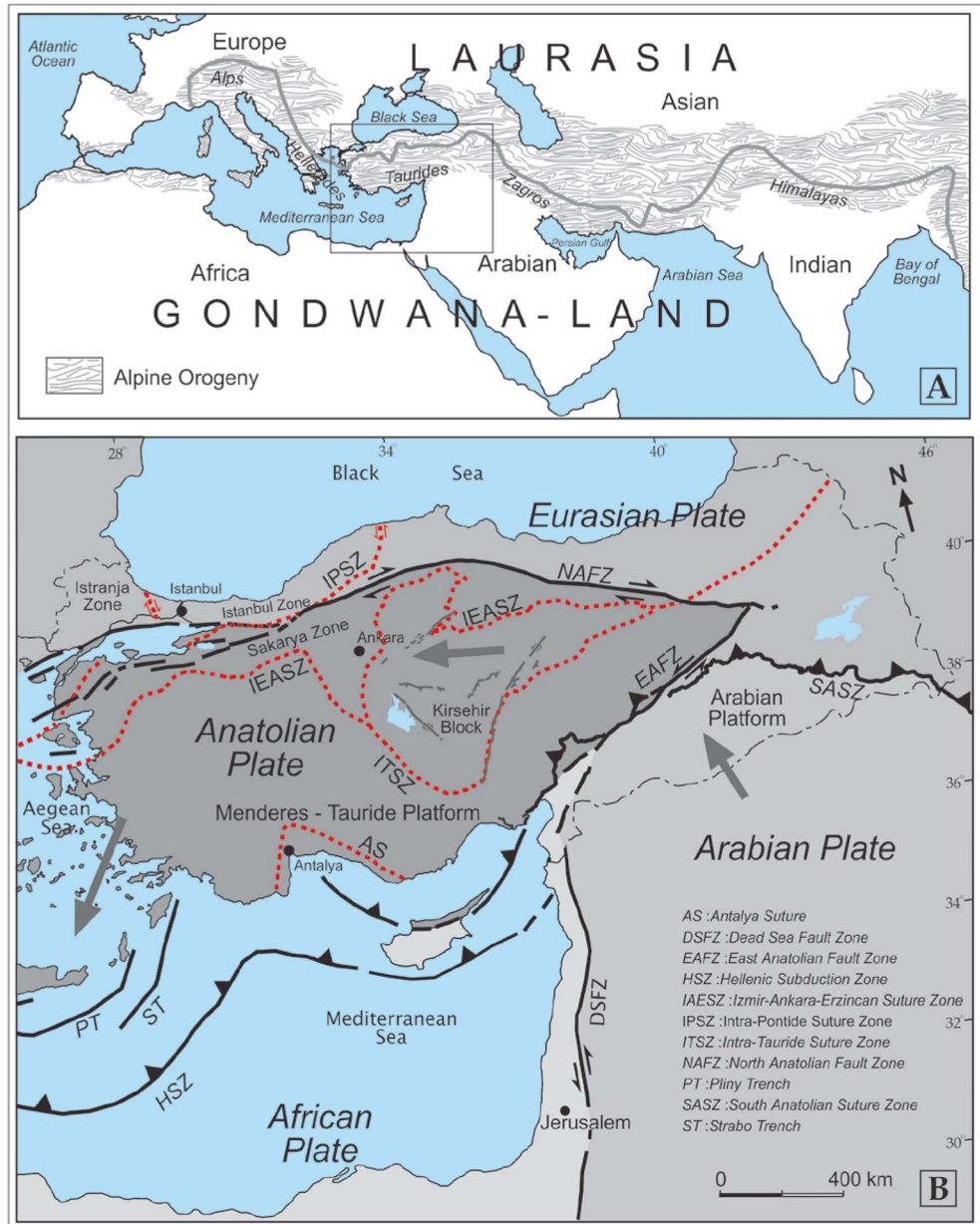
Figure 1. (a) Spatial distribution of the Alpine-Himalayan orogeny. (b) Map of Turkey and its surroundings showing principal plate boundaries. Red dashed heavy lines indicate paleotectonic suture zones and separate continental crusts. Large arrows indicate relative motion along fault zones or motion of plates. Barbs showing the hanging wall side (modified from *Okay and Tüysüz* [1999] and *Isik* [2009]).

In this paper, we investigate the Savcili Fault Zone (SFZ) in central Turkey, which represents another prominent intraplate fault system of the Anatolian plate. *Sengor and Yılmaz* [1981] considered thrust faults within central Turkey as inner deformation events that occurred due to collision of the Pontides and the Anatolide-Tauride Platform. Consequently, north-south shortening created retrocharriage structures in the Anatolides during the late Eocene. This thrusted brittle slices of the Kırsehir massif over Eocene units in a northerly direction, which is represented by the Savcili Thrust Zone [*Oktay*, 1981].

Alternatively, the SFZ has been interpreted as a thrust zone that formed due to the compression in central Anatolia throughout Paleogene resulting from the collision of the Central Anatolian Crystalline Complex (CACC) with the central Pontides [*Gorur et al.*, 1998; *Lefebvre et al.*, 2013]. The CACC is the largest exposed
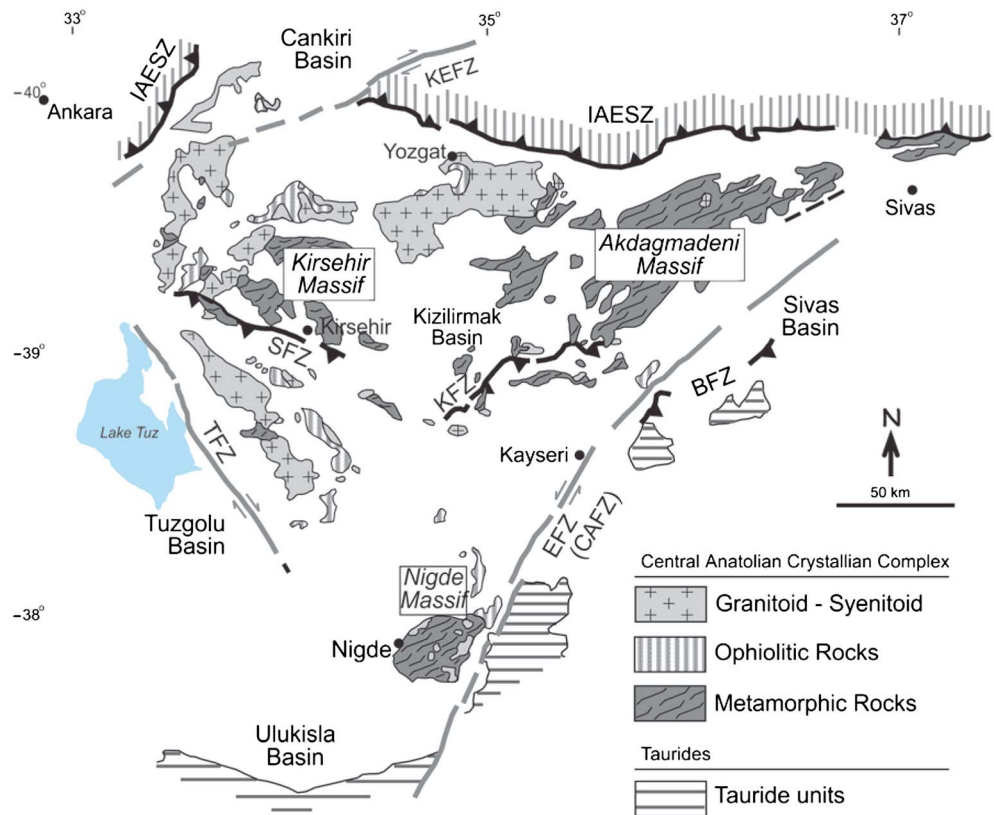
Figure 2. Simplified geologic map of central Turkey, showing distribution of major rock units in the central Anatolian crystalline complex and some major structures (modified after *Isik* [2009]). Abbreviations: BFZ: Bunyan Fault Zone, EFZ: Ecemis Fault Zone, IAESZ: Izmir-Ankara-Erzincan Suture Zone, KEFZ: Kirikkale-Erbaa Fault Zone, KFZ: Kursunludag Fault Zone, and SFZ: Savcili Fault Zone.

metamorphic domain in Turkey. Based on paleomagnetic studies of Cretaceous plutons within the CACC, *Lefebvre et al.* [2013] showed evidence for three internally coherent domains of the CACC with significantly different vertical axis rotations: (1) in the northeast, the Akdag-Yozgat block, (2) in the northwest, the Kirsehir-Kirikkale block (KKB), and (3) in the southwest, the Agacoren-Avanos block (AAB). The SFZ separates the KKB from AAB and represents a left-lateral transpressional zone, accommodating ~30° of counterclockwise rotation between the KKB and AAB. The rotation and internal deformation in the CACC occurred throughout most of the Paleocene-Eocene [*Lefebvre et al.*, 2013]; however, constraining the timing of relative rotation between the KKB and AAB accurately is not possible because there are no available paleomagnetic data of Paleogene age.

While earlier studies relate the SFZ to regional compression, more recent investigations suggest that the SFZ is part of a detachment fault system related to an extensional regime [*Genc and Yürür*, 2004, 2010; *Yurur and Genc*, 2006]. This makes the age of the SFZ is more controversial. According to *Oktay* [1981] and *Seymen* [1984], the SFZ has been active since late Eocene. This is, however, debatable as other fault zones (Kursunludag and Bunyan) being correlated with the SFZ are covered by Miocene sediments, rendering the SFZ a paleotectonic structure [*Goncuoglu et al.*, 1993; *Dirik and Goncuoglu*, 1996].

The purpose of this study is threefold: (1) to delineate the character and kinematics of the regionally important SFZ; (2) to better constrain its age by combined Rb-Sr and Ar-Ar dating techniques of illite-bearing fault gouge samples; and (3) to discuss the significance of the SFZ in the tectonic evolution of the eastern Mediterranean region, based on field observations, microstructural, and radioisotope data. In addition to understanding geometric and kinematic constraints, unraveling the temporal evolution of trust belts as presented by the SFZ provides useful information on regional processes that drive postcollisional tectonics of the Neo-Tethyan suture zone. Knowledge on the timing of brittle faulting in the central Anatolian thrust belts is particularly needed because previous estimates are inconsistent and have mostly been determined from

contrasting field interpretations and sedimentary records or from radiometric dating of associated features (such as high-pressure/low-temperature metamorphism, granite intrusions).

Isotopic dating of upper crustal brittle deformation events is a difficult task, unlike dating of minerals from deeper ductile shear zones. This is due to incomplete syntectonic mineral recrystallization in the brittle regime [*van der Pluijm et al.*, 2001, 2006]. It has been argued that fault gouge consists of a mixture of newly formed 1 M (authigenic) [see *Srodon and Eberl*, 1984] illite within the brittle fault zone and detrital 2 M muscovite or metamorphic illite inherited from the undeformed protolith. The presence of 2 M phyllosilicates has been attributed to temperatures (below 200°C) during brittle faulting, which precludes complete recrystallization and hence isotopic resetting of the 2 M mineral phase [*van der Pluijm et al.*, 2001, 2006; *Haines and van der Pluijm*, 2008; *Duvall et al.*, 2011]. However, fault gouges can also contain 100% fault-formed illite, as a result of complete dissolution-recrystallization of K-bearing detrital minerals during significant fluid flow events controlled by faulting [*Uysal et al.*, 2006, 2011; *Mutlu et al.*, 2010; *Zwingmann et al.*, 2011; *Uysal et al.*, 2011; *Yamasaki et al.*, 2013]. Isotopic age data of major fault zones in Turkey is limited [e.g., *Uysal et al.*, 2006; *Mutlu et al.*, 2010; *Hetzel et al.*, 2013], with no direct isotopic age data available for the SFZ until this study. The present study is the first to attempt combining Rb-Sr and Ar-Ar dating techniques for 100% illite fault gouge and to determining the timing of fault reactivation episodes in intraplate fault systems in central Turkey. In addition, we present stable isotope data of fault gouge illites to constrain the source and evolution of fluids during brittle faulting in intraplate fault systems.

2. Regional Geological Setting

The Alpine-Himalayan orogenic system resulted from the closure of the Neo-Tethyan Oceans and deformation of their margins since the Late Cretaceous (Figure 1a). Turkey represents a particular part of the eastern Mediterranean region typified by intense plate movements. Turkey is positioned on the boundary between the Eurasian and African/Arabian plates, which is characterized by the presence of several major continental fragments and suture zones. The Strandja, Istanbul, and Sakarya Zones in northern Turkey represent the Laurasian continent, whereas the Kirsehir Block, the Menderes-Tauride Platform, and the southeastern part of Turkey (Arabian platform) form parts of the continental crust of Gondwana [*Sengor and Yılmaz*, 1981; *Sengor and Natalin*, 1996; *Okay and Tüysüz*, 1999; *Moix et al.*, 2008] (Figure 1b). Relative motions of Eurasian, African, and Arabian plates resulted in ocean closure, continental collisions associated with widespread metamorphism and magmatism and formation of sedimentary basins. Collision of the Eurasian plate with the African and Arabian plates along the suture zone in southeast Turkey created the Anatolian microplate, which moves southwest along the North Anatolian and East Anatolian Fault Zones [*Sengor et al.*, 1985; *Faccenna et al.*, 2006] (Figure 1b).

The study area is located within the Kirsehir Block, which is bordered by the remnants of the northern branch of the Neo-Tethyan Ocean, also known as Izmir-Ankara-Erzincan Suture Zone and intra-Tauride suture. The existence and position of the latter, however, is controversial [*Sengor and Yılmaz*, 1981; *Poisson et al.*, 1996; *Yaliniz and Goncuoglu*, 1996]. The Kirsehir Block consists of metamorphic rocks, ophiolitic units, granitoid-syenitoid intrusions, and sedimentary rocks from Late Mesozoic and Cenozoic sedimentary basins. Crystalline rocks of the Kirsehir Block, referred to as Central Anatolian Crystalline Complex (CACC) [*Goncuoglu et al.*, 1991], are also known as Kirsehir, Akdagmadeni and Nigde Massifs (Figure 2). Metamorphic rocks consisting of gneiss, amphibolite, marble, and schist represent the oldest tectonostratigraphic units of the Kirsehir Block. A Late Cretaceous (91-84 Ma) age has been reported for the peak metamorphism [*Whitney et al.*, 2003; *Whitney and Hamilton*, 2004]. These metamorphic units are overlain by the Central Anatolian Ophiolites [*Goncuoglu et al.*, 1991], which occur as mélange and a fore-arc accretionary prism [*Capan and Floyd*, 1985; *Kocyigit*, 1991]. Limited age data are available for the ophiolites [e.g., *Yaliniz et al.*, 2000]. The metamorphic and ophiolitic units are intruded by granitoids which ages between 110 Ma and 54 Ma [e.g., *Ayan*, 1963; *Ataman*, 1972; *Yaliniz et al.*, 1999; *Kadioglu et al.*, 2003; *Ilbeyli et al.*, 2004; *Koksal et al.*, 2004; *Isik et al.*, 2008; *Boztug et al.*, 2009a, 2009b]. More recent studies suggest ages of approximately 65 Ma [*Isik et al.*, 2008, and references therein]. Geochemical data classify these granitoids as metaaluminous to peraluminous rocks that represent syncollisional and postcollisional magmatism [e.g., *Boztug*, 2000; *Ilbeyli et al.*, 2004; *Koksal et al.*, 2004; *Goncuoglu*, 2009]. Alternatively, some of intrusions have been related to a regional extension during the latest Cretaceous [*Isik et al.*, 2008; *Isik*, 2009].

Crystalline basement of central Turkey is covered by rocks from various sedimentary basins (e.g., Ulukisla Basin, Tuzgolu Basin, Haymana Basin, Cankiri Basin, Yozgat-Sorgun Basin, Sivas Basin, and Kizilirmak Basin) (Figure 2). While the majority of sediment deposition in these basins occurred during Tertiary, sedimentation in some basins was initiated in the Maastrichtian [*Oktay*, 1981; *Poisson et al.*, 1996; *Gorur et al.*, 1998; *Cemen et al.*, 1999; *Derman et al.*, 2000; *Clark and Robertson*, 2005; *Jaffey and Robertson*, 2005]. These basins are interpreted to have developed in arc-related (fore arc and intra-arc) and collision-related (peripheral foreland) basin systems [*Gorur et al.*, 1998]. However, this interpretation is highly controversial due to geochemical analyses indicating an extensional volcanic activity (i.e., Ulukisla Basin) [*Clark and Robertson*, 2002, 2005; *Alpaslan et al.*, 2004, 2006]

3. Savcili Fault Zone

The Savcili Fault Zone constitutes one of the most prominent structures in central Turkey and is located in the western part of the Kirsehir Block. The SFZ was originally mapped as "the Savcili Thrust Fault" [*Oktay*, 1981]; however, later work by *Isik et al.* [2010a, 2010b] classified a number of reverse faults placing Mesozoic Kirsehir metamorphic and plutonic rocks over the Paleogene sedimentary units as the "Savcili Fault Zone". This fault zone is most likely continued by the Kursunludag Fault Zone in the central and eastern part of the Kirsehir Block [*Dirik and Goncuoglu*, 1996] (Figure 2).

3.1. Geometry

The SFZ represents discrete zones of exhumed individual reverse faults across a broad area. Despite faults being relatively discontinuous on the surface, they are interpreted as being kinematically linked at depth. The Savcili Fault Zone has a west-northwest to east-southeast strike and can be seen between Hirfanli and Kirsehir (Figure 3). The zone is exposed for more than 50 km in length and several hundred meters wide depending on Neogene cover units and structural complexities along the fault zone. A number of parallel to subparallel individual fault traces of the SFZ occur with an anastomosing geometry. The basement (metamorphic rocks and granitoid intrusions) and the early Tertiary sedimentary rocks are thrust over Paleocene sedimentary units. Faulting occurs as reverse and low-angle thrust faults in both in Mesozoic and Paleocene units. Cataclastic zones are seen clearly within the fault zone. In areas with well-preserved fault slip surfaces, the fault core and damage zone are visible. Individual fault surfaces commonly strike WNW/NW with a SW dip but less frequently strike NE and dip to SE. The detachment fault separating the ophiolite mélange from the metamorphic rocks is older than the SFZ [*Lefebvre et al.*, 2011, 2012] (Figure 3). Observable strike-slip and normal faults are still active and hence younger than the SFZ [*Kocyigit*, 2003].

3.2. Host Rocks

Intense deformation during faulting affected the metamorphic, granitoid basement, and Paleocene sedimentary rocks. The metamorphic rocks are dominated by marble, gneiss, schist, amphibolite, and quartzite, and are strongly folded and fractured, whereas the intensity of granitoid deformation is variable depending on its primary texture and mineral content. Quartz-rich varieties show more intense fracturing, while those having abundant feldspars have been altered strongly allowing the formation of clay-rich fault gouge. Paleogene units start at the bottom with a thick clastic unit (up to 1000 m) dominated by red to bordeaux, poorly sorted conglomerate and conglomerate with boulder, which deposited above the basement rocks with a nonconformity. When regionally correlated a middle-late Paleogene to early Eocene age is estimated for this rock succession. Indeed, with regard to the exhumation age of granitoid [see *Boztug and Jonckheere*, 2007] that supplied gravels to the conglomerates the age of the terrestrial sediments might be late Paleocene-early Eocene. These clastic sediments in turn are overlaid by clastic and fossil-bearing carbonate rocks of Late Lutetian-Bartonian (middle Eocene) in age. Sediments that cover these fossil-bearing units are interpreted to have a late Eocene-middle Miocene age based on the regional correlation [*Kara and Dönmez*, 1990; *Kara*, 1991; *Goncuoglu et al.*, 1994]. Similarly, Paleogene sedimentary rocks have been subjected to intense brittle deformation.

3.3. Fault Rocks and Microstructures

Individual fault-segments within the SFZ consist of two structural domains; the fault core and damage zone, collectively known as cataclastic zone [*Isik et al.*, 2010a, 2010b]. The cataclastic zone is characterized by brittle fractures and fault rocks. Fault cores are 0.10 to 1 m in width and are mostly associated with fault surface and likely host the majority of the fault's displacement. Fault surfaces have a curved geometry and include
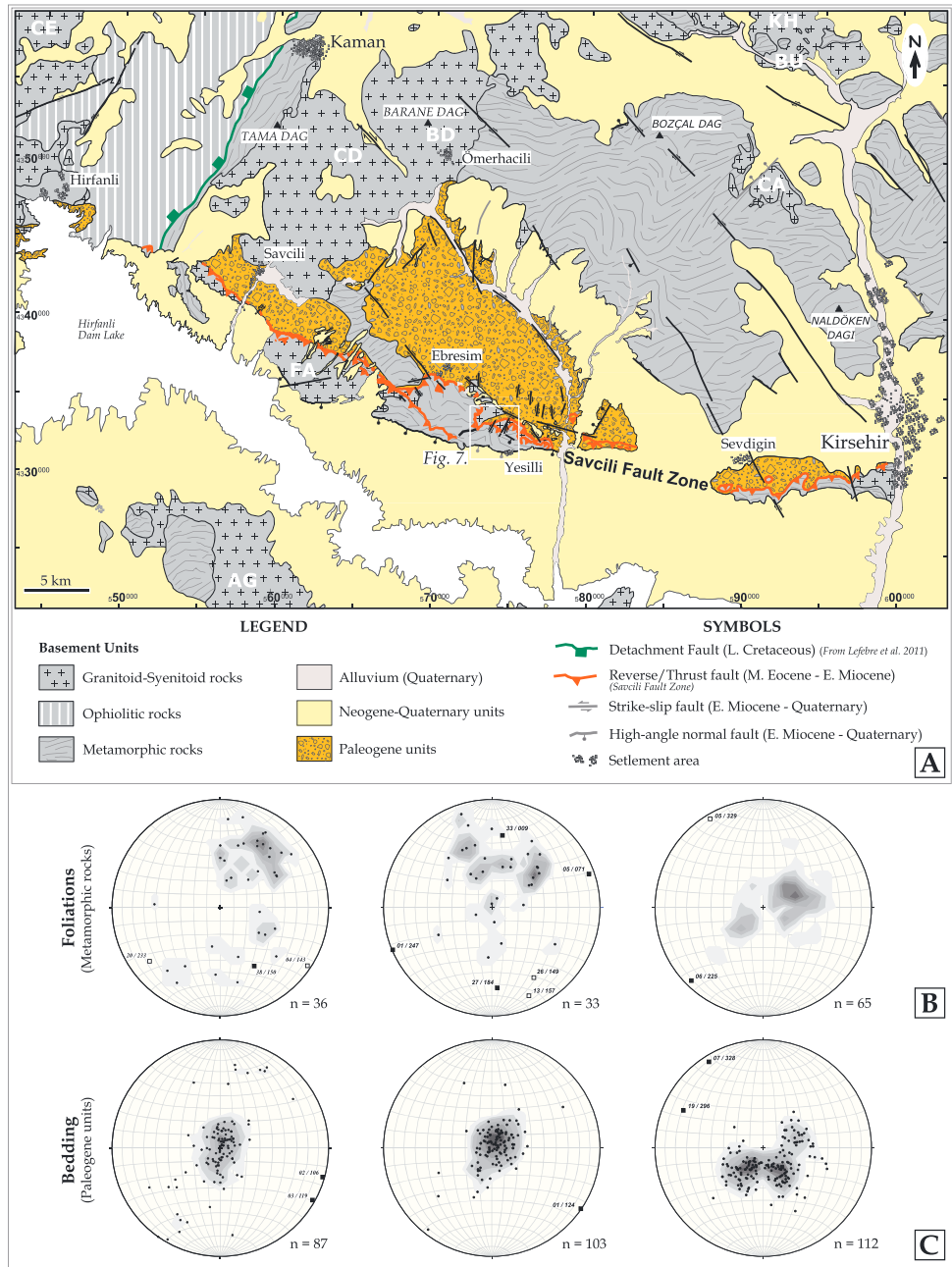
Figure 3. (a) Geologic map of the Savcili Fault Zone and its surroundings. *Pluton Abb.* AG: Agacoren, BD: Baranedag, BU: Buzlukdag, CA: Cayagzi, CD: Cefalikdag, CE: Celebi, FA: Fakili, and KH: Karahidir. (b) Equal area projection of poles (poles (small filled circles) to foliation measurements with counters in domains of metamorphic rocks. (c) Equal area projection of poles (small filled circles) to bedding measurements with counters in domains of Paleogene units. Contour intervals correspond to 2, 4, 6, 8, 10, 12, 14, and 16% orientation concentration per unit area. Boxes on diagrams indicate orientation of fold hinges. Note that filled boxes define fold hinges related to the SFZ. *n* showing number of measurements.

slickenlines and brittle kinematic indicators (Figures 4c and 4d). The fault core contains R and P shears, which occasionally cut and slightly displace the slip surface. Such structures are observed on tens of centimeters scale and commonly occur in sets defining lens geometry. The fault cores grade into the damage zones with sharp or gradual contact. The damage zones extend up 10–50 m from the fault core and grade into the undeformed rock. They consist of variable fractured rocks, fault rocks, and preserved protolith surrounded by fault rocks. Cataclastic zones in the SFZ have asymmetric cores and damage zones with respect to fault planes.
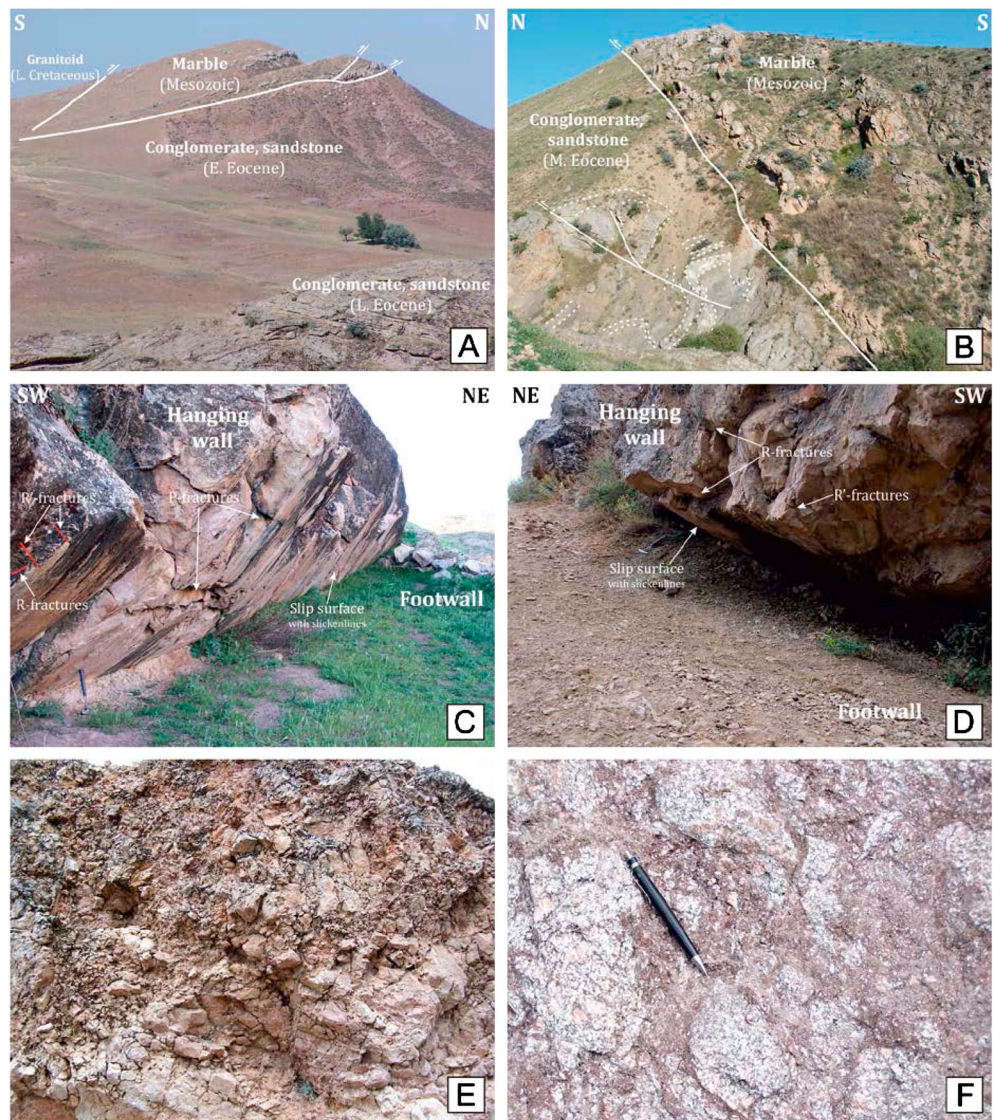
Figure 4. Photographs of features observed along the SFZ. (a) Panoramic view of the SFZ where basement rocks (marble, granitoid) are thrust over early Eocene sedimentary rocks. Bold lines are faults. (b) General view of the cataclastic zone. Note that middle Eocene sedimentary units fractured and folded below the marble. Dashed lines indicate bedding of sedimentary rocks. Bold lines represent fault trace. (c, d) Close-up view of the fault scarps with fault surfaces. (e, f) Close-up of the brecciated marble and granodiorite. Note that breccias contain angular to subangular fragments of marble (Figure 4e) and granodiorite fragments ranging from several millimeters to centimeters.

The fault rocks in the SFZ consist of cataclasites, gouges, and clast- or matrix-supported breccias (Figures 4e and 4f). These rocks differ from one structural domain to another. The contact between fault rocks is sharp or gradual. Fault rocks derived from granitoid rock are wider and pervasive compared to those derived from cataclastic sedimentary rocks and marbles. Cataclasites are the closest fault rocks to slip surfaces (slickenside) and are 1–5 cm thick. The rocks have subangular to rounded clasts (both mineral and rock fragments) surrounded by a brown, fine-grained matrix (Figure 5a). While the cataclasite appears mostly massive in hand specimen, in thin section it occurs with transgranular microscopic fractures and thin zones of very fine-grained materials that are mostly parallel to the slip surface (cataclastic foliation). Gouges are also close to slip surfaces and occur as fine-grained, beige, light green, and gray incohesive fault rocks, which are composed of matrix and clasts (Figure 5b). The matrix material consists of finely-grained rock and mineral fragments as well as secondary clay, chlorite, and calcite. Clasts are usually represented by quartz, feldspar, and calcite showing subrounded crystal fragments. Some of the clasts within the gouge reveal reworked
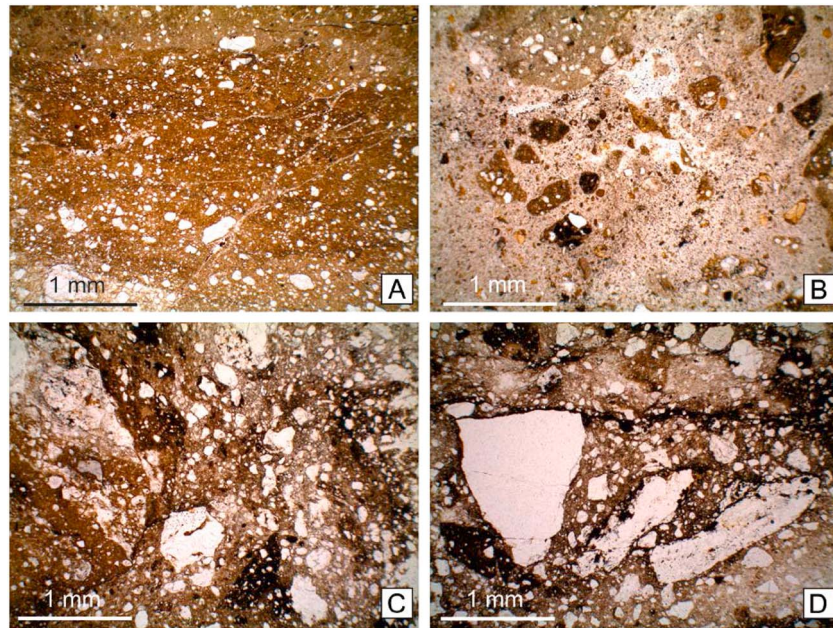
Figure 5. Photomicrographs of fault rocks within the cataclastic zones illustrating fault rocks. (a) Cataclasite, (b) fault gouge, and (c, d) microbreccias. Note angular to subrounded fragments floating in a variable amount of matrix material. All photomicrographs are in plane-polarized light.

cataclasite suggesting an episodic evolution of displacement. Brecciation is common in the cataclastic zones. In thin sections, clast- or matrix-supported breccias include angular to subrounded crushed rock fragments (Figures 5c and 5d) and secondary minerals containing clay, chlorite, and calcite. Clast size varies between 1 mm and 15 mm. Both the clasts and matrix in fault rocks consist of material derived from the protolith rocks (granodiorite, conglomerate, and sandstone) and a lesser amount of crystalline calcite representing the cement precipitated in veins and voids (Table 1).

3.4. Kinematics

Cataclastic zones of the SFZ are characterized by pervasive brittle deformation as seen from fault striae, fault surfaces (slickenside), cataclastic foliation, shear fractures, and jointing. Fault surfaces and striations are good indicators of paleostress vectors. Fault slip surfaces are commonly preserved in marbles that are polished and have iron coatings, or less frequently, calcite coatings with well-developed slickensides and slickenlines. Slickensides are corrugated with slip-parallel lineations and brittle kinematic indicators (V or crescentic markings, steps, fractures, and trailed materials) [e.g., *Hancock*, 1985; *Doblas*, 1998; *Caglayan*, 2010] showing top to the NE and NW sense of brittle deformation shearing.

Fault slip data required for estimating the paleostress tensor were collected from the SFZ and analyzed using the programs, FaultKinWin version 1.1 [*Allmendinger*, 2001] and Win-Tensor [*Delvaux and Sperner*, 2003]. The results are presented in Figure 6. The mean orientations of the slickensides and fault striae are 116°/40° and 37°/175°, respectively (Figure 6a). The mean value is consistent with the trend of the SFZ. The tangent diagram displays a relatively uniform southward sense of slip for the footwall of the SFZ (Figure 6b). The mean *P* and *T* axes provide a first-order approximation of the infinitesimal maximum shortening and maximum extension directions, respectively, indicating a sense of slip on a reverse/thrust fault for the SFZ (Figures 6c and 6d). This sense of slip on the reverse/thrust fault indicates a horizontal, almost N-S orientation for shortening axes (3) and a nearly vertical orientation for extensional axes (1) (Figures 6c and 6d). Shortening and extension axis contouring and Bingham moment tensor summation define a vertical extension axis trending 075.6° and a horizontal shortening axis trending 181.7° (Figure 6e).

These results are consistent with those inferred from using the program Win-tensor. Fault slip analyses reveal that the principal stress axes, σ_1, σ_2, and σ_3, were oriented 05°/183°, 11°/274°, and 78°/069°,

Table 1. Petrographic Description and Mineral Contents of Savcili Fault Rock Samples

Sample	Lithology/ Protolith	Fault Rock Type	Whole-Rock Mineralogy by XRD	Phylosilicate Mineralogy (<2 μm Size Fraction) by XRD
10SAV-1	Granite	Breccia	Calcite, quartz, and plagioclase	Chlorite, smectite, and trace mica
10SAV-2	Granite	Breccia	Quartz, plagioclase, and minor chlorite	Mixed-layered chlorite-smectite, minor chlorite, and smectite
10SAV-3A	Granite	Cataclasite	Quartz, plagioclase, K-Feldspar, mica, chlorite, and calcite	Mixed-layered chlorite-smectite, and minor mica
10SAV-3B	Granite	Cataclasite	Quartz, plagioclase, chlorite, calcite, and mica	Smectite, zeolite, chlorite, and mixed-layered chlorite-smectite
10SAV-4	Sandstone	_	Quartz, calcite, plagioclase, and K-feldspar	Smectite, zeolite, chlorite, and mixed-layered chlorite-smectite
10SAV-5	Calc-silicatic gneiss	Cataclasite	Quartz, calcite, and kaolinite	Kaolinite, mica, and smectite
10SAV-6	Sandstone	Breccia	Quartz, plagioclase, K-feldspar, and minor calcite	Smectite, kaolinite, and mica
10SAV-7	Sandstone	_	Quartz, K-feldspar, plagioclase, calcite, and minor mixed-layered chlorite-smectite	Smectite, kaolinite, and mica
10SAV-8A	Gneiss	_	Quartz, plagioclase, chlorite, mixed-layered chlorite-smectite, and calcite	Mica, chlorite, and mixed-layered chlorite-smectite
10SAV-8B	Gneiss	Breccia	Quartz, plagioclase, chlorite, mixed-layered chlorite-smectite, calcite, and mica	Mica and chlorite
10SAV-10	Gneiss	_	Quartz, calcite, plagioclase, mixed-layered chlorite-smectite, and minor chlorite	Smectite, mica, and chlorite
10SAV-11	Gneiss	_	Quartz, plagioclase, mica, and K-feldspar	Mica and chlorite
10SAV-12	Gneiss	_	Quartz, mica, plagioclase, chlorite, and K-feldspar	Chlorite and mica
10SAV-14	Pegmatite	_	Quartz, K-feldspar, and plagioclase	Smectite, kaolinite, and mica
10SAV-15	Gneiss	_	Quartz, plagioclase, K-feldspar, mica, calcite, chlorite, and minor amphibole	Mica, chlorite, and amphibole
10SAV-16A	Gneiss	_	Plagioclase, pyroxene, and K-feldspar	Smectite and mica
10SAV-17	Monzonite	_	Quartz, hornblende, plagioclase, mica, and chlorite	Smectite, illite, chlorite, and amphibole
10SAV-18	Foliated granite	Proto cataclasite	Plagioclase, mixed-layered chlorite-smectite	Mica and chlorite
10SAV-19	Foliated granite	Proto cataclasite	K-feldspar, plagioclase, quartz, chlorite, and minor hornblende	Chlorite and mica
10SAV-20	Gneiss	_	Quartz, chlorite, plagioclase, calcite, and mica	Mica and chlorite
10SAV-24	Gneiss	_	K-feldspar, plagioclase, quartz, and minor calcite	Chlorite
10SAV-25	Gneiss	_	Quartz, plagioclase, and minor chlorite	Illite, chlorite, and kaolinite
10SAV-31	Granite	_	Quartz, chlorite, and minor calcite	Chlorite and mica
10SAV-37	Gneiss	_	Quartz, plagioclase, and mica	Mica and chlorite
10SAV-38	Granodiorite	Fault gouge	Quartz, dolomite, plagioclase, and K-feldspar	Illite and minor chlorite
10SAV-39	Granodiorite	Fault gouge	Quartz, calcite, and kaolinite	Illite and kaolinite
10SAV-41	Sandstone/ Conglomera	Fault gouge	Quartz, calcite, and minor illite	Illite and minor chlorite
10SAV-42	Gabro	_	Amphibole and pyroxene	Smectite and amphibole

respectively (Figure 6e). The σ_1 axis is close to horizontal and σ_3 axis show a plunge close to 80°, indicating the SFZ is a typical reverse/thrust zone. In addition to the orientations of principal stresses, results of fault slip analyses include a parameter, called stress ratio (ϕ, R) [*Angelier*, 1984; *Orife and Lisle*, 2003]. The stress ratio defines the shape of the stress ellipsoid. The stresses in the study area give rise to R value above 0.55 (0.79). The stress tensor and R value define pure to radial compressive (σ_3 vertical, $0.625 < R < 0.875$) regime along the SFZ.

The SFZ strikes on average N64°W with a sinuous shape in map view (Figure 3). Faults along the SFZ generally dip 40° to the SSW (Figure 6). Most of the fault striations moderately plunge southwestward and southeastward on SW and SE dipping planes (Figure 6). Data from the SFZ indicate a compressional regime characterized by reverse motions in response to an approximate N-S horizontal direction of the greatest principal stress (σ_1) (Figure 6).

Structural data for fault surfaces (Figure 6) correlate with the position of the axis of some folds as shown in Figure 3. Analysis of deformation structures and overprinting relationships in metamorphic rocks in the region reveals multiple phases of ductile deformation [*Isik et al.*, 2011]. Ductile deformation structures include
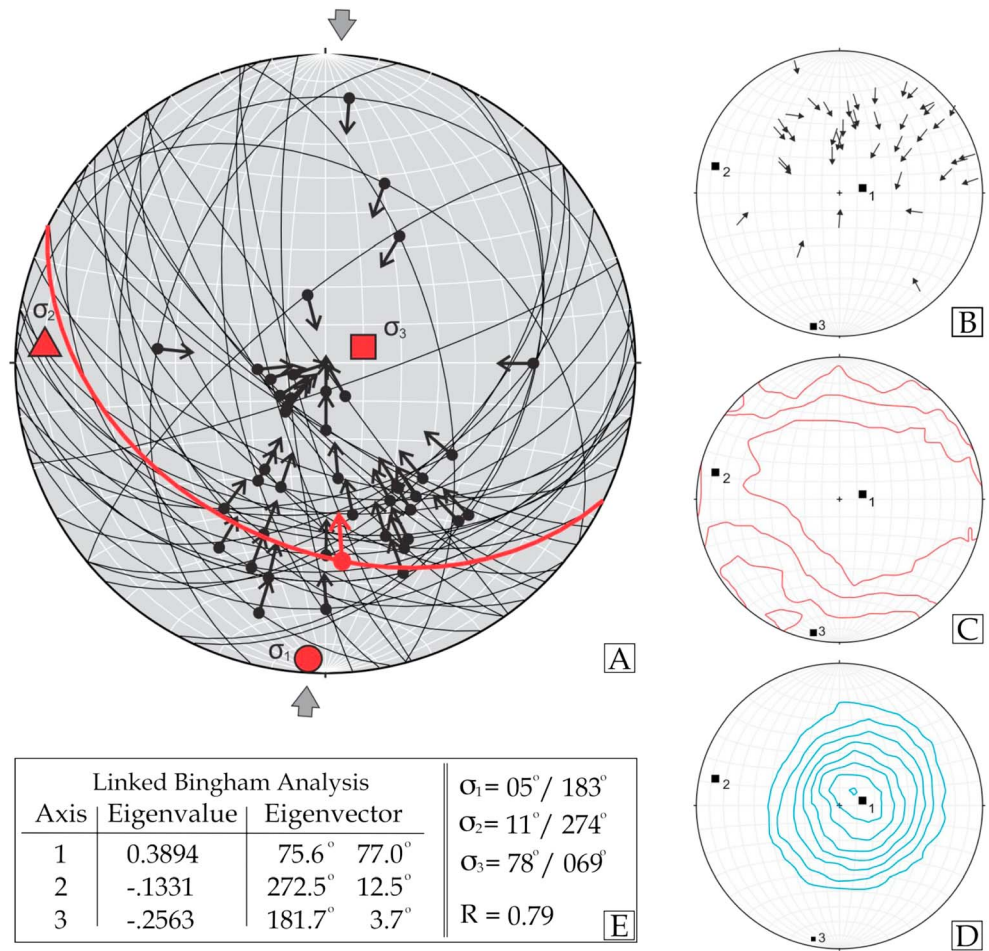
Linked Bingham Analysis			$\sigma_1 = 05°/183°$
Axis	Eigenvalue	Eigenvector	$\sigma_2 = 11°/274°$
1	0.3894	75.6° 77.0°	$\sigma_3 = 78°/069°$
2	-.1331	272.5° 12.5°	R = 0.79
3	-.2563	181.7° 3.7°	E

Figure 6. Results of kinematic analysis of the SFZ plotted on lower hemisphere, equal area net. (a) Slickenside and slicken-lines orientations (*n* = 41). Great circles represent slickenside orientations. Arrows within circle indicate the movement of the hanging walls. Bold great circle and bold arrow correspond to average fault and slip line orientation of the SFZ. (b) Tangent lineation diagram for the entire fault slip surfaces that arrows show footwall movement. Black squares indicate three kinematic axes. (c) Kamb contours of shortening (*P* axes). (d) Kamb contours of extension (*T* axes). (e) A dialog box showing there linked Bingham axes (1, 2, 3), eigenvalues, and eigenvectors. Note that results of σ_1, σ_2, and σ_3 axes and *R* value are also given.

recumbent, moderately inclined, upright horizontal, and gently plunging folding at various scales. Regionally, some of these folding-related structures are probably associated with evolution of the SFZ (Figure 3b). Likewise, Paleogene units are also folded. These folds are generally steeply inclined and gently plunging. The orientation of the fold axis obtained from the measurement of the bedding for these units is consistent with the orientation of some of the metamorphic rocks (Figure 3c). This indicates that both metamorphic and sedimentary rocks have been affected by the same deformation event, and hence, the folding is related to the evolution of the Savcili Fault Zone.

Paleomagnetic data from Turkey allow a quantitative estimation of latitudinal drift and rotations around vertical axes [e.g., *Tatar et al.*, 1996; *Gursoy et al.*, 1997, 1998; *Platzman et al.*, 1998; *Kissel et al.*, 2003; *Lefebvre et al.*, 2013]. Although paleomagnetic data from different regions of central Turkey are scattered, the estimated amount of counterclockwise rotation in the Neogene, from 12 Ma to the present, is approximately 50° [*Platzman et al.*, 1998]. *Kissel et al.* [2003] suggested the Kirsehir block rotated by ~ 25° in a counterclockwise sense during the Neogene. Although our fault kinematic results point to approximately N-S compression, paleomagnetic results in central Turkey indicate a postmovement with the average counterclockwise rotation of about 25°. Thus, central Turkey has been affected by NE-SW compression at least until early Miocene time.
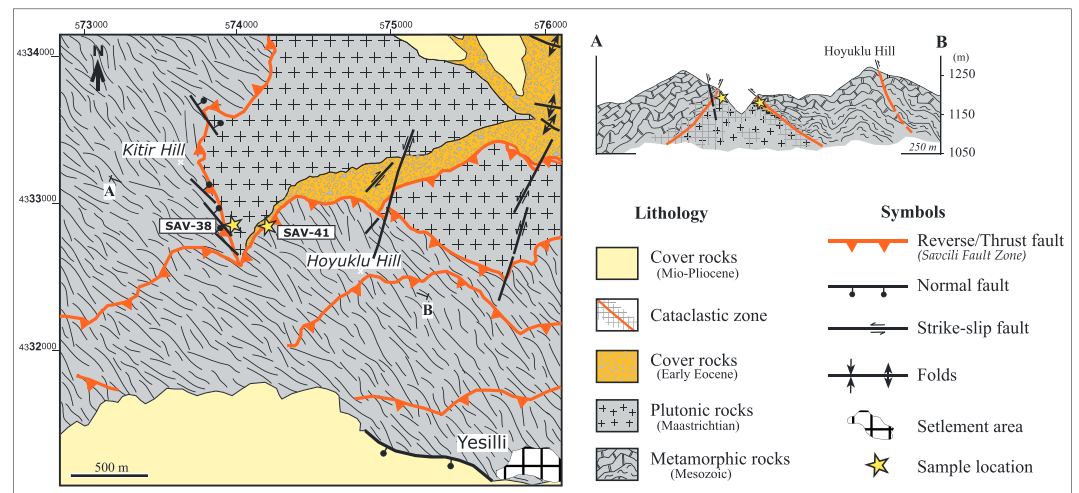
Figure 7. (a) Geological map and (b) cross section along the SFZ showing the localities of fault gouge samples that were used for Rb-Sr and Ar-Ar dating, stable isotope, and trace element analyses. Stars represent location of samples.

4. Petrography and Clay Mineralogy of Fault Rocks and Protolith

4.1. Sampling and Analytical Procedures

Petrographic analyses were carried out by thin section studies and X-ray diffraction (XRD) on whole-rock samples and clay separates (<2 μm). The XRD analyses were carried out on a Bruker Advance MK III X-Ray diffractometer with Bragg-Brentano geometry and CuKα radiation, operated at 40 kV and 30 mA at a scanning rate of 1°2θ/min and 0.05°/step. The samples were prepared for separation of the clay fraction by gently crushing the rocks to sand size, followed by disaggregation in distilled water using an ultrasonic bath. Different clay size fractions were obtained by centrifugation, and the decanted suspensions were placed on a glass slide. To ensure no detrital contamination, samples were centrifugally separated and rigorously analyzed with XRD. Samples showing contamination with detrital illite-muscovite were either discarded from analysis or separated to finer micron fractions. Following XRD analysis of air-dried samples, the oriented clay-aggregate mounts were placed in an ethylene-glycol atmosphere at 30–40°C overnight prior to additional XRD analyses. To determine illite content in illite-smectite mixed-layer clays, the method of differential two theta ($\Delta2\theta$) was used, with an analytical error of about ± 5% [*Moore and Reynolds*, 1997].

To obtain an age estimate on fault movements along the SFZ and to determine the source and evolution of fluids in relation to faulting, two fault gouge samples have been selected in the footwall of the SFZ for isotopic dating. The location of these samples is presented in Figure 7. Fault rocks in sample *SAV-38* domain are greenish, gray, and beige in color and mostly composed of matrix-supported breccias and gouges. Sample *SAV-38* was derived from a granodiorite host rock exposed within the cataclastic zone (Figure 8a). The exposure of *SAV-41* domain is characterized by a 5 m thick cataclastic zone between the undeformed marbles of the hanging wall and clastic rocks of the footwall. The fault gouge sample of the *SAV-41* domain comes from a conglomerate and sandstone of early Eocene cover unit and characterized by reddish-, brownish-colored gouge (Figure 8b).

4.2. Results of Petrography and Clay Mineralogy

Petrographic and mineralogic descriptions of deformed fault rocks and undeformed protolith are summarized in Table 1. Results of whole-rock and clay mineralogy by XRD analysis of samples collected along the Savcili Fault Zone are presented in Table 1. Samples from locations *SAV-38* and *SAV-41* are clay-rich fault gouges containing authigenic illite and minor chlorite in the <2 μm clay size fraction (Table 1). Smaller-size fractions of <1 μm consist entirely of illite. The XRD 001 peak position of the illite does not change after ethylene glycol treatment, which is indicative of absence of smectite clays [*Srodon and Eberl*, 1984]. Illite crystallinity (IC) value of the <2 μm illite fraction is approximately 0.65 $\Delta2\theta$ and 0.70 $\Delta2\theta$ for samples *SAV-38* and *SAV-41*, respectively, which is indicative of illite precipitation under diagenetic conditions with
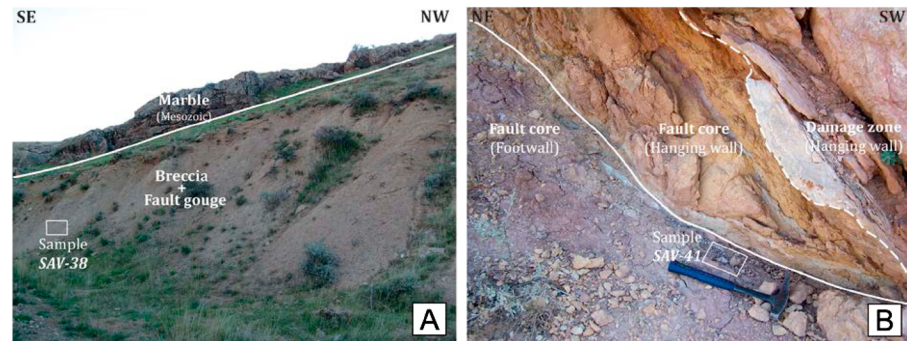
Figure 8. (a) Outcrop photo of sample *SAV-38* location showing cataclastic zone. Note that granodiorite in the footwall completely destroyed and turned into fault rocks. (b) Outcrop photo of sample *SAV-41* location showing the fault core and adjacent damage zone domains of hanging wall and the fault core domain of the footwall. Bold lines indicate fault trace. Dashed line indicate margins of fault core and damage zone domains.

temperatures less than 250℃ [*Merrriman and Frey*, 1999]. IC values of 1–0.5 µm, 0.5–0.2 µm, and 0.2 µm illite fractions are around of around 0.80 $\Delta 2\theta$, 0.90 $\Delta 2\theta$, and 0.54 $\Delta 2\theta$, and 1.10 $\Delta 2\theta$, 0.15 $\Delta 2\theta$, and 0.74 $\Delta 2\theta$ for samples *SAV-38* and *SAV-41*, respectively.

Petrographic and mineralogical data clearly show that clay mineral assemblages from the fault gouges and their parent rocks are significantly different. The protolith of the fault gouge sample for *SAV-38* and *SAV-41* are granodiorite from the basement and Tertiary sandstone, respectively. In thin section, these samples contain small angular to rounded crushed crystal or rock fragments and matrix material. Both parent rocks are partially altered from which the clay fractions of <2 µm consist of inherited mica, smectite, chlorite, and mixed-layered chlorite-smectite but contain no authigenic illitic clay minerals (Table 1).

5. Rb-Sr Dating of Fault Gouge

5.1. Rb-Sr Methodology

For the Rb-Sr dating, illitic clay separates were leached for 15 min at room temperature in 1 N distilled HCl [*Clauer et al.*, 1993]. Leachate and residue were separated by centrifuging. The residue was rinsed repeatedly with milli-Q water, dried, and reweighed. Clay separates were analyzed in two separate batches. Leachate, residue, and untreated samples from the first batch were spiked with ^{85}Rb-^{84}Sr mixed tracer and dissolved in a mixture of distilled HF and HNO$_3$, while the second batch were measured directly by Thermo X-series 1 quadrupole inductively coupled plasma–mass spectrometer (ICP-MS) with precision better than 0.5% (1σ). The Sr-enriched fraction was separated using cation exchange resins. Sr isotopic ratios were measured on a VG Sector-54 thermal ionization mass spectrometer in the Radiogenic Isotope Laboratory at University of Queensland. Sr was loaded in TaF$_5$ and 0.1 N H$_3$PO$_4$ on a tantalum or tungsten single filament. Sr isotopic ratios were corrected for mass discrimination using ^{86}Sr/^{88}Sr = 0.1194. Long-term (6 years) reproducibility of statically measured NBS Standard Reference Material (SRM) 987 (2σ; n = 442) is 0.710249 ± 28. More recent dynamically measured SRM 987 had ^{86}Sr/^{88}Sr ratios of 0.710222 ± 20 (2σ; n = 140). Rb-Sr isochron ages were calculated using the ISOPLOT program [*Ludwig*, 2003].

5.2. Results of Rb-Sr Dating

Rb-Sr data for the untreated, acid-leached residues and leachates of clay fractions from Savcili fault gouge samples are presented in Table 2 and on Figure 9. The data of untreated and residues for 2-1, <2, 1–0.5, 0.5–0.2, and <0.2 µm illite size fractions of sample *SAV-41* show well-defined linear relationships corresponding to an isochron age of 22.9 ± 1.3 Ma, (Figure 9a). The initial ^{87}Sr/^{86}Sr ratio of 0.710.16 ± 0.00036 is greater than ^{87}Sr/^{86}Sr ratios of the coexisting acid-leachable components ranging narrowly between 0.709181 and 0.709104 (Table 2 and Figure 9a). Leachates of these clay fractions do not plot on the isochron line suggesting that the acid-leachable components are not in isotopic equilibrium with the illite. Plotting data of only acid-leached residues gives an analytically indistinguishable age of 22.4 ± 1.5 Ma (initial ^{87}Sr/^{86}Sr = 0.71053 ± 0.00051) (Figure 9b). The data of untreated clays, their acid-leached residues and leachates for 2-1, <2, 1–0.5, 0.5–0.2, and <0.2 µm clay size fractions of sample *SAV-38* together with

Table 2. [87]Rb-[86]Sr Data for the Untreated, Leachates, and Acid-Leached (Residues) Clay Fractions From the Savcili Fault Gouges[a]

Sample	Size Fraction (μm)	^{87}Rb/^{86}Sr	Rb (ppm)	Sr (ppm)	^{87}Sr/^{86}Sr ± 2σ
10SAV-38	2-1U	14.40	251	38.3	0.718906 ± 10
10SAV-38	2-1R	21.11	277	38.3	0.723042 ± 7
10SAV-38	2-1L	0.26	1.38	12.9	0.709584 ± 7
10SAV-38	< 2U	20.44	244	21.2	0.722147 ± 9
10SAV-38	< 2R	30.90	230	13.1	0.728513 ± 10
10SAV-38	< 2L	0.46	1.47	3.67	0.709575 ± 7
10SAV-38	1-0.5U	26.38	317	35.0	0.726263 ± 10
10SAV-38	1-0.5R	47.60	269	16.5	0.737420 ± 7
10SAV-38	1-0.5L	0.41	1.79	12.0	0.709811 ± 7
10SAV-38	0.5-0.2U	37.56	314	24.2	0.732701 ± 7
10SAV-38	0.5-0.2R	81.81	275	9.79	0.757122 ± 8
10SAV-38	< 0.2U	10.32	302	84.5	0.714760 ± 9
10SAV-38	< 0.2R	67.10	277	12.0	0.745774 ± 9
10SAV-38	< 0.2L	0.34	8.36	68.8	0.709562 ± 7
10SAV-41	2-1U	5.23	270	150	0.711702 ± 9
10SAV-41	2-1R	5.00	171	101	0.712205 ± 9
10SAV-41	2-1L	0.08	0.737	22.2	0.709104 ± 7
10SAV-41	< 2U	6.28	248	114	0.711938 ± 7
10SAV-41	< 2R	9.95	245	71.8	0.713540 ± 10
10SAV-41	< 2L	0.13	1.08	21.0	0.709117 ± 9
10SAV-41	1-0.5U	7.03	303	125	0.712287 ± 7
10SAV-41	1-0.5L	0.08	0.669	18.4	0.709120 ± 7
10SAV-41	0.5-0.2U	14.73	318	62.7	0.715089 ± 9
10SAV-41	0.5-0.2R	20.18	293	42.5	0.717174 ± 9
10SAV-41	0.5-0.2L	0.14	0.852	14.4	0.709181 ± 9
10SAV-41	< 0.2U	18.64	290	45.1	0.715665 ± 7
10SAV-41	< 0.2R	51.73	290	16.4	0.726947 ± 7
10SAV-41	< 0.2L	0.06	0.646	21.5	0.709116 ± 9

[a]U=untreated, R=residue, and L=leachate.

leachates of sample *SAV-41* define a linear relationship from which the slope yields a Rb-Sr age of 40.9 ± 1.5 Ma (initial ^{87}Sr/^{86}Sr = 0.70958 ± 0.0060) (Figure 9c). The Rb-Sr isotope data of only acid-leached residues (excluding <0.2 μm size fraction) for *SAV-38* show a linear relationship corresponding to a similar age of 39.4 ± 1.5 Ma (initial ^{87}Sr/^{86}Sr = 0.71116 ± 0.00094) (Figure 9d).
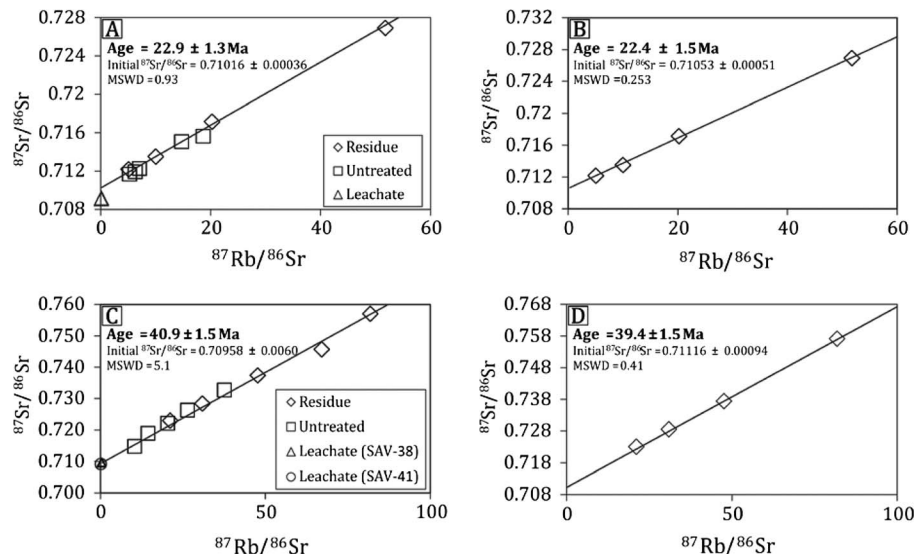

Figure 9. Rb-Sr isochrons of leachate-residue-untreated clay fractions for illite samples ((a, b) for *SAV-41* and (c, d) for *SAV-38*) from the Savcili fault gouge samples.
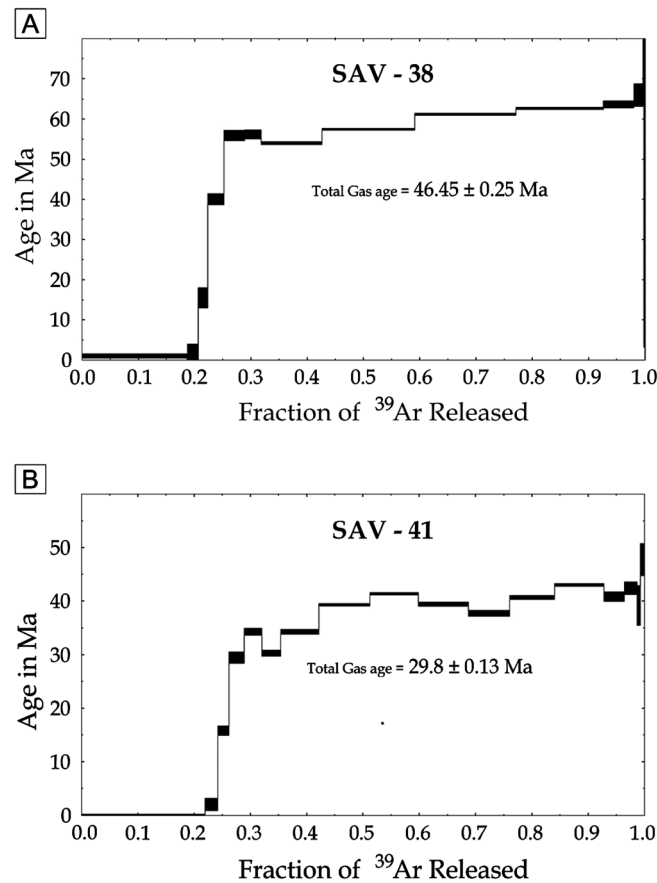
Figure 10. Results of ^{40}Ar-^{39}Ar step heating for vacuum-encapsulated illite from the Savcili fault gouges.

6. Ar-Ar Dating of Fault Gouge

6.1. Ar-Ar Methodology

Two samples were dated by the Ar-Ar method at the University of Michigan. Illitic clay samples were resuspended in 1 mL of deionized water, spun-down at 10,000 rpm in a microcentrifuge and carved into a ~1 mm pellet following decanting. To avoid loss of ^{39}Ar due to recoil, clay pellets were placed in 1 mm ID-fused silica vials prior to being sent for neutron irradiation for 90 MWh in medium flux locations of the McMaster Nuclear Reactor (hole 8C for irradiation 1, 8A for irradiation 2). Following irradiation, samples were attached to a laser fusion system, broken under a 1×10^{-8} Torr vacuum and step-heated in situ using a defocused beam from a 5 W Coherent *Innova* continuous Ar-ion laser operated in multiline mode. Argon isotopes were then analyzed using a VG1200S mass spectrometer equipped with a Daly detector operated in analogue mode using methods by *Hall* [2013]. Ages in this study are calculated relative to an age of 520.4 Ma for standard hornblende MMhb-1 [*Samson and Alexander*, 1987].

6.2. Results of Ar-Ar Dating

Results of ^{40}Ar/^{39}Ar geochronology for 0.5–0. 2 μm and <0.2 μm clay size fractions of samples *SAV-38* and *SAV-41*, respectively are presented in Figure 10. The Ar-release spectra do not display plateaus, which is due to the Ar recoil effect. The low-temperature ^{39}Ar recoil loss is 19% and 22% for *SAV-38* and *SAV-41*, respectively. Such significant ^{39}Ar recoil losses are typical for illite grains with illite crystallinity values of 0.90 $\Delta 2\theta$ and 0.74 $\Delta 2\theta$ (for 0.5–0.2 μm and <0.2 μm clay size fractions for samples *SAV-38* and *SAV-41*, respectively [see *Dong et al.*, 1995; *Hall et al.*, 1997]. Degree of ^{39}Ar loss has been shown to be inversely proportional to the mean packet thickness (i.e., illite crystallinity) [*Dong et al.*, 1995]. Following the release of ^{39}Ar at low temperatures, all spectra show a high step associated with enhanced mobility and excess loss of ^{39}Ar caused by formation point defects during recoil. Therefore, we use total gas ages for dating of fine-grained illitic clay minerals from the fault gouges, which are equivalent to K-Ar ages [*Dong et al.*, 1995].

Illite of 0.5–0.2 μm size fraction of sample *SAV-38* produced total gas ages of 46.45 ± 0.25 Ma (Figure 10a), whereas <0.2 μm clay size fractions of sample *SAV-41* gave a total gas age of 29.08 ± 0.13 Ma (Figure 10b).

7. Stable Isotope Analysis of Fault Gouge

7.1. Stable Isotope Methodology

Illitic clay minerals were analyzed for their stable isotope (δ^{18}O and δD) compositions. Oxygen was extracted from illitic clays for isotope analyses using a CO_2 laser and BrF_5 [*Sharp*, 1990]. Oxygen isotope values are reported in per mil relative to Vienna SMOW (VSMOW) and normalized to the international quartz standard (NBS-28) using a value of 9.6‰. Replicate values for NBS-28 quartz ($n = 6$) analyzed with the samples had values that varied by less than 0.2‰. Samples and standards were heated overnight in a muffle furnace to 170°C

Table 3. Stable Isotope Data of Illites From Savcili Fault Gouges

Sample	Grain Size (μm)	δ^{18}O (SMOW) (‰)	δD (SMOW) (‰)
10SAV-38	<2	9.4	−68.8
10SAV-38	2-1	8.8	−65
10SAV-38	1-0.5	9.3	−59.7
10SAV-38	0.5-0.2	8.8	−72.9
10SAV-41	2-1	9.7	−73.3
10SAV-41	1-0.5	9.6	−70.1
10SAV-41	0.5-0.2	8. 8	−78.3
10SAV-41	<0.2	9.4	−71.6

prior to loading into the vacuum extraction line to remove any adsorbed water. The samples were then evacuated for approximately 6 h and left overnight in a vapor of BrF5. Blank BrF_5 was run until the yield was less than 0.1 μmol oxygen. Oxygen was passed through a fluorine getter (in-line Hg diffusion pump) and converted to CO_2 by a graphite furnace; yields were recorded and CO_2 analyzed on a Geo20–20 mass spectrometer at the Institute of Geological and Nuclear Sciences Limited (GNS) Laboratory, New Zealand. Hydrogen isotope analysis of clays was similarly conducted at the GNS Laboratory using a HEKAtech high-temperature elemental analyzer coupled with a GV Instruments IsoPrime mass spectrometer. All samples were pyrolyzed at 1450℃ in silver capsules and analyzed in triplicate. All isotope ratios are reported in per mil relative to VSMOW, with an analytical uncertainty of ±2‰ (1σ). Results are normalized to international standards IAEA–CH–7, NBS30, and NBS22, with reported δD values of −100‰, −66‰, and −118‰, respectively.

7.2. Results of Stable Isotope Analysis

The stable isotope data of different clay size fractions of Savcili fault gouge illites are shown in Table 3 and Figure 11. Stable isotope compositions of illite separates from fault gouge samples *SAV-38* and *SAV-41* are very similar, particularly with δ^{18}O values in a narrow range between 8.8 and 9.7‰ (Table 3, Figure 11). Fault gouge illites from *SAV-38* and *SAV-41* exhibit similar δD values ranging from −60 to −78‰ (Table 3, Figure 11).

8. Trace Element Analysis of Fault Gouge

8.1. Trace Element Methodology

For trace element analysis, clay samples were dissolved with a mixture of HF and nitric acids on a hotplate, then evaporated to dryness, refluxed twice with nitric acid and dissolved in 2 N nitric acid. Aliquots of the solutions were spiked with internal standards, diluted and analyzed on a Thermo X-series 1 quadrupole inductively coupled plasma–mass spectrometer (ICP-MS) in the Radiogenic Isotope Laboratory at the University of Queensland. Sample preparation and analytical procedures used were similar to those of *Eggins et al.* [1997], except that Tm was not used as an internal standard and duplicate low-pressure digestions of W-2, US Geological Survey diabase standard, were used as the calibration standard. BIR-1, AGV1, AGV2, and G2 were run as unknown. The ^{156}CeO/^{140}Ce ratio for the run was 0.016. Long-term precision (relative standard deviation) was based on duplicate analyses of the duplicate digestions of AGV1, while precision for the run was based on five duplicate analyses of W-2 which were better than 3% for most elements, except for Li, Zn, Mo, Cd, and Cs, which ranged between 5% (Li, Cd, and Cs) and 15% (Zn).

8.2. Results of Trace Element Analysis

Trace element data of different clay size fractions from the fault gouge samples are given in Table 4. Trace element concentrations of the acid-leached residues and the untreated illites are similar, while leachable phases are more depleted in all trace elements (except Ni). Trace element ratios for illite separates from the fault gouge samples are also presented in Table 4. Such element ratios are used commonly to characterize the source compositions of clastic sedimentary rocks [e.g., *Taylor and McLennan*, 1985]. Untreated illites, acid-leached residues, and leachable
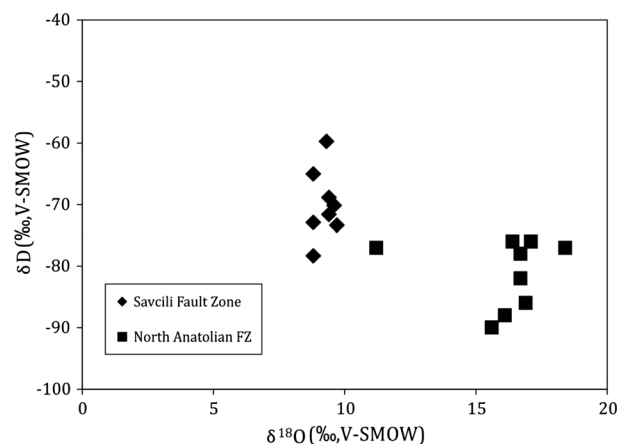

Figure 11. Stable isotope results of illites from the Savcili fault gouges in comparison to fault gouge illites from the NAFZ.

Table 4. Trace Element Data (ppm) of Illites From the Savcili Fault Gouges[a]

	38U_ <2	38U_2-1	38U_1-0.5	38U_0.5-0.2	38U_ <0.2	41U_ <2	41U_2-1	41U_1-0.5	41U_0.5-0.2	41U_ <0.2	38R_ <2	38R_2-1	38R_1-0.5	38R_0.5-0.2	38R_ <0.2
Li	u.d.l.[b]	12.8	17.8	2.97	9.42	11.3	11.9	12.4	9.64	8.69	u.d.l.	4.23	10.4	2.39	2.51
Be	8.11	6.93	6.98	6.54	6.62	3.81	4.48	4.99	4.70	3.99	5.95	4.88	5.08	4.65	4.14
Sc	3.34	3.31	3.99	3.78	3.21	6.80	7.95	8.53	8.18	6.96	2.88	3.29	3.09	2.99	2.61
Ti	1417	2491	1212	675	408	1120	2409	1862	770.3	182	1362	2229	1210	666	400
V	105	101	97.1	93.1	77.3	68.1	79.8	86.2	79.3	62.2	100	91.2	97.0	89.7	75.3
Cr	19.4	24.5	23.5	25.5	23.3	33.5	36.6	39.0	38.1	31.4	19.2	22.5	25.5	23.4	22.9
Co	2.82	4.76	7.13	6.72	5.80	4.22	4.50	4.95	4.83	3.98	2.24	3.99	5.81	5.31	3.49
Ni	59.9	64.9	66.1	67.9	67.9	68.1	67.1	64.1	62.2	62.8	29.9	31.7	31.6	31.3	32.6
Rb	244	251	317	314	302	248	270	303	318	290	230	277	269	275	277
Sr	21.2	38.3	35.0	24.2	84.5	114	150	125	62.7	45.1	13.1	38.3	16.5	9.79	12.0
Y	5.42	7.79	4.87	3.07	2.35	7.99	12.06	11.7	6.93	2.80	4.10	5.30	2.76	1.63	1.07
Zr	8.66	9.53	6.89	6.38	6.14	9.91	15.38	15.4	12.2	8.73	8.78	8.32	6.56	5.53	5.39
Nb	7.42	14.1	6.48	3.16	1.66	6.27	13.9	10.6	4.21	0.772	7.14	13.5	6.48	3.14	1.68
Mo	1.49	1.04	0.973	0.833	18.7	0.823	0.456	0.419	0.239	0.796	0.646	1.03	0.880	0.745	1.27
Sn	35.5	36.9	46.9	54.9	135	181	46.8	48.5	45.1	39.2	19.1	24.7	30.2	26.9	72.3
Sb	0.393	0.425	0.392	0.338	0.381	2.21	2.85	2.97	2.28	1.54	0.353	0.430	0.378	0.309	0.282
Cs	19.1	15.7	22.8	27.2	32.1	34.9	35.7	42.9	53.3	56.8	17.6	17.2	21.5	24.9	30.7
Ba	35.0	54.5	62.4	74.5	106	204	751	483	281	216	17.9	22.4	15.4	20.7	24.2
La	41.8	57.3	28.9	13.8	6.99	73.8	89.3	74.5	31.7	8.03	36.5	49.6	17.2	9.82	5.82
Ce	77.8	106	54.4	26.6	13.6	141	167	142	60.1	15.9	71.5	97.4	42.2	20.3	11.0
Pr	8.45	11.3	5.76	2.83	1.46	14.0	16.5	13.9	5.91	1.52	7.35	9.55	3.52	2.03	1.16
Nd	26.1	35.7	19.3	9.56	4.98	45.0	53.2	44.7	18.9	4.89	22.3	31.2	11.8	6.77	3.83
Sm	4.11	5.54	2.97	1.53	0.848	7.00	8.48	7.09	2.99	0.787	3.43	4.61	1.80	1.02	0.579
Eu	0.625	0.899	0.545	0.297	0.175	1.12	1.34	1.16	0.510	0.134	0.522	0.802	0.330	0.187	0.108
Gd	2.358	3.197	1.718	0.936	0.592	3.98	4.93	4.17	1.82	0.532	1.845	2.426	1.025	0.568	0.337
Tb	0.289	0.392	0.211	0.123	0.083	0.458	0.587	0.512	0.249	0.083	0.224	0.276	0.128	0.071	0.042
Dy	1.268	1.763	1.014	0.614	0.462	2.01	2.73	2.48	1.32	0.488	0.964	1.196	0.606	0.337	0.212
Ho	0.186	0.275	0.184	0.115	0.090	0.321	0.472	0.453	0.263	0.104	0.137	0.204	0.109	0.063	0.040
Er	0.526	0.758	0.479	0.312	0.248	0.756	1.19	1.20	0.741	0.311	0.393	0.490	0.289	0.172	0.111
Tm	0.070	0.105	0.068	0.047	0.039	0.100	0.168	0.176	0.115	0.051	0.052	0.064	0.042	0.025	0.017
Yb	0.474	0.691	0.439	0.308	0.260	0.625	1.08	1.14	0.752	0.341	0.348	0.401	0.259	0.164	0.110
Lu	0.076	0.106	0.062	0.044	0.039	0.089	0.154	0.166	0.110	0.051	0.054	0.056	0.035	0.023	0.016
Hf	0.541	0.601	0.483	0.444	0.400	0.574	0.806	0.805	0.674	0.518	0.508	0.544	0.461	0.397	0.367
Ta	0.336	0.654	0.347	0.182	0.100	0.530	1.15	0.900	0.380	0.074	0.327	0.740	0.343	0.179	0.098
Tl	1.51	1.53	1.75	1.70	1.44	1.35	1.50	1.67	1.75	1.51	1.41	1.59	1.72	1.63	1.39
Pb	13.9	21.9	19.0	17.9	17.1	8.16	13.0	12.2	7.43	3.38	7.56	9.55	10.1	8.61	5.78
Th	21.5	26.1	18.1	12.7	9.14	44.1	49.0	46.6	23.6	7.58	16.8	19.7	11.9	7.73	4.71
U	4.39	6.30	4.61	3.69	4.33	3.17	3.80	3.32	2.03	2.09	2.95	4.30	2.99	2.16	1.64
La/Sc	12.5	17.3	7.3	3.7	2.2	10.8	11.2	8.7	3.9	1.2	12.7	15.1	5.6	3.3	2.2
La/Th	1.9	2.2	1.6	1.1	0.8	1.7	1.8	1.6	1.3	1.1	2.2	2.5	1.4	1.3	1.2
Th/Sc	6.5	7.9	4.5	3.4	2.8	6.5	6.2	5.5	2.9	1.1	5.8	6.0	3.9	2.6	1.8
Cr/Th	0.9	0.9	1.3	2.0	2.5	0.8	0.7	0.8	1.6	4.1	1.1	1.1	2.1	3.0	4.9

Table 4. (continued)

	41R_ <2	41R_2-1	41R_1-0.5	41R_0.5-0.2	41R_ <0.2	38L_ <2	38L_2-1	38L_1-0.5	38L_0.5-0.2	38L_ <0.2	41L_ <2	41L_2-1	41L_1-0.5	41L_0.5-0.2	41L_ <0.2	PAAS
Li	7.69	11.7	11.3	8.34	12.6	u.d.l.	u.d.l.	14.9	0.741	3.56	1.71	0.983	1.11	1.10	2.26	
Be	2.86	3.94	3.94	3.33	2.93	1.68	1.43	1.58	1.78	2.42	0.992	0.994	0.937	0.921	0.998	
Sc	6.60	6.04	6.47	7.02	6.44	0.181	0.548	0.464	0.451	0.598	0.092	0.351	0.306	0.337	0.370	
Ti	1088	2692	1913	760	174	0.421	0.725	0.877	0.700	3.20	0.330	0.332	0.284	0.238	0.262	
V	65.5	87.0	86.4	73.8	58.1	0.277	0.507	0.325	0.338	1.32	1.054	0.637	0.748	0.619	1.09	
Cr	33.6	41.3	40.1	33.7	27.1	0.190	0.483	0.376	0.426	0.663	0.299	0.347	0.381	0.478	0.454	
Co	3.71	4.64	4.76	4.39	3.70	0.267	2.25	1.15	1.16	2.12	0.155	0.123	0.131	0.104	0.088	
Ni	31.8	31.4	30.0	29.9	30.6	78.1	82.6	79.4	76.8	84.5	85.9	79.1	76.3	72.0	76.4	
Rb	245	171	204	293	290	1.47	1.38	1.79	1.66	8.36	1.08	0.737	0.669	0.852	0.646	
Sr	71.8	101	85.7	42.5	16.4	3.67	12.9	12.0	10.6	68.8	21.0	22.2	18.4	14.4	21.5	
Y	7.07	7.07	7.67	5.61	2.40	1.16	1.66	1.05	0.92	1.17	0.621	0.966	0.689	0.421	0.231	
Zr	8.94	15.6	14.7	11.2	7.56	0.270	0.220	0.181	0.184	0.376	0.737	0.339	0.258	0.268	0.909	
Nb	6.13	15.4	11.0	4.21	0.743	0.003	0.004	0.002	0.001	0.002	0.003	0.004	0.002	0.000	u.d.l.	
Mo	0.245	0.447	0.360	0.183	0.103	0.079	0.079	0.022	0.013	1.43	0.035	0.009	0.007	0.007	0.025	
Sn	66.4	50.7	26.9	25.3	23.2	0.798	1.88	4.13	2.61	9.91	6.78	1.07	0.727	0.789	0.995	
Sb	1.98	3.06	2.89	2.11	1.35	0.007	0.022	0.005	0.003	0.017	0.019	0.006	0.014	0.005	0.017	
Cs	33.6	34.9	39.3	47.8	56.1	0.139	0.165	0.199	0.152	0.549	0.137	0.057	0.058	0.074	0.062	
Ba	42.0	123	62.6	68.6	65.1	13.8	25.1	33.5	42.9	80.3	132	489	324	173	139	
La	72.5	51.4	44.5	26.8	7.39	1.44	2.09	1.59	1.28	1.03	1.03	0.799	0.513	0.295	0.126	
Ce	135	120	107	52.6	14.2	3.34	4.71	3.37	2.73	2.35	2.85	2.39	1.74	1.06	1.05	
Pr	13.2	11.2	9.43	5.06	1.39	0.426	0.555	0.385	0.306	0.277	0.273	0.259	0.159	0.085	0.036	
Nd	42.4	37.0	31.0	16.2	4.43	1.55	2.10	1.42	1.14	1.06	1.03	1.04	0.628	0.327	0.145	
Sm	6.54	6.03	5.13	2.53	0.694	0.364	0.480	0.299	0.237	0.248	0.228	0.269	0.171	0.084	0.037	
Eu	1.05	0.963	0.863	0.440	0.124	0.063	0.109	0.074	0.058	0.068	0.035	0.033	0.023	0.012	0.002	
Gd	3.61	3.37	2.98	1.49	0.454	0.339	0.456	0.267	0.216	0.246	0.221	0.292	0.192	0.096	0.045	
Tb	0.411	0.403	0.375	0.199	0.070	0.050	0.066	0.039	0.033	0.039	0.030	0.042	0.027	0.015	0.007	
Dy	1.77	1.86	1.82	1.07	0.406	0.256	0.348	0.216	0.186	0.234	0.151	0.222	0.154	0.086	0.048	
Ho	0.284	0.319	0.336	0.212	0.088	0.037	0.063	0.042	0.036	0.046	0.026	0.039	0.027	0.017	0.009	
Er	0.671	0.801	0.890	0.605	0.268	0.120	0.177	0.110	0.102	0.133	0.062	0.098	0.071	0.047	0.027	
Tm	0.086	0.114	0.131	0.094	0.044	0.018	0.026	0.017	0.016	0.021	0.008	0.014	0.010	0.007	0.005	
Yb	0.549	0.735	0.847	0.618	0.291	0.123	0.176	0.118	0.107	0.144	0.052	0.087	0.071	0.053	0.031	
Lu	0.078	0.105	0.120	0.089	0.043	0.021	0.027	0.017	0.016	0.021	0.008	0.012	0.010	0.007	0.005	
Hf	0.507	0.831	0.765	0.604	0.454	0.012	0.009	0.010	0.012	0.016	0.035	0.013	0.012	0.012	0.046	
Ta	0.519	1.27	0.924	0.369	0.071	0.001	u.d.l.	u.d.l.	u.d.l.	u.d.l.	u.d.l.	u.d.l.	u.d.l.	0.001	u.d.l.	
Tl	1.31	1.58	1.63	1.61	1.50	0.009	0.011	0.018	0.018	0.030	0.007	0.008	0.008	0.007	0.007	
Pb	6.42	11.5	9.75	5.57	2.44	5.56	10.8	7.90	7.90	10.8	1.55	1.78	1.84	1.42	0.876	
Th	46.1	46.9	44.5	20.9	6.76	3.19	4.67	3.87	3.41	4.06	0.584	1.07	0.709	0.536	0.419	
U	1.93	3.40	2.65	1.30	0.591	1.21	1.61	1.48	1.35	2.54	0.991	0.614	0.627	0.591	0.705	
La/Sc	11.0	8.5	6.9	3.8	1.1	8.0	3.8	3.4	2.8	1.7	11.2	2.3	1.7	0.9	0.3	2.4
La/Th	1.6	1.1	1.0	1.3	1.1	0.5	0.4	0.4	0.4	0.3	1.8	0.7	0.7	0.6	0.3	2.6
Th/Sc	7.0	7.8	6.9	3.0	1.0	17.6	8.5	8.3	7.6	6.8	6.3	3.0	2.3	1.6	1.1	0.9
Cr/Th	0.7	0.9	0.9	1.6	4.0	0.1	0.1	0.1	0.1	0.2	0.5	0.3	0.5	0.9	1.1	7.5

[a]U = untreated, R = residue, and L = leachate, (PAAS = Archean Average Shale [Taylor and McLennan, 1985]).
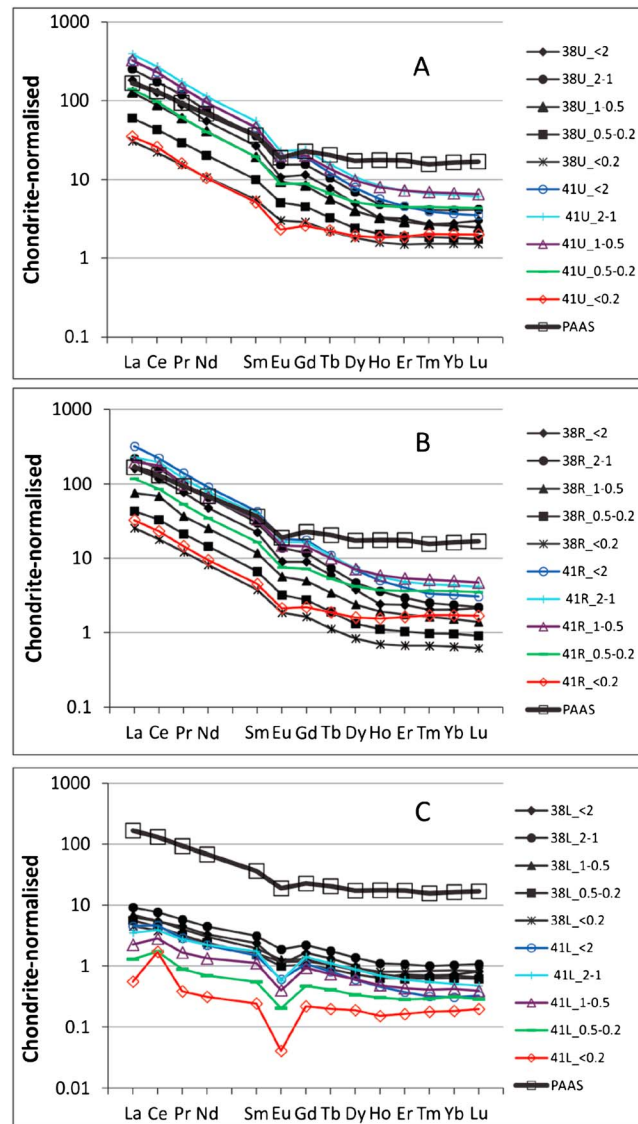[b]u.d.l. = under detection limit.

Figure 12. Rare earth element data of illites from the Savcili fault gouges.

phases show significantly high Th/Sc and La/Sc ratios and low La/Th and Cr/Th ratios compared to those of Post-Archean Average Shale (PAAS). Chondrite-normalized rare earth element (REE) patterns of untreated illites and their acid-leached residues and leachates from the fault gouges are shown in Figures 12a–12c, respectively. In addition, the REE pattern of Post-Archean Average Shale (PAAS) [*Taylor and McLennan*, 1985] is included in all REE diagrams. The acid-leached residues and the untreated illites are depleted in heavy REE relative to PAAS (Figures 12a and 12b). Chondrite-normalized $(La/Lu)_c$ ratios of illite residues and untreated illites are higher than the $(La/Lu)_c$ ratio of PAAS (10), while REE patterns of the leachates are mostly parallel to the pattern of PAAS.

9. Discussion

9.1. Interpretation of Rb-Sr Ages

Illitic clay minerals from the Savcili fault gouges display well-developed linear data arrays on Rb-Sr isochron diagrams (Figure 9). We interpret such linear relations as representing complete isotopic equilibration of the entire authigenic clay mineral population during episodic fluid flow triggered by faulting. X-ray diffraction patterns of clay size fractions from the fault gouges show that clays of all d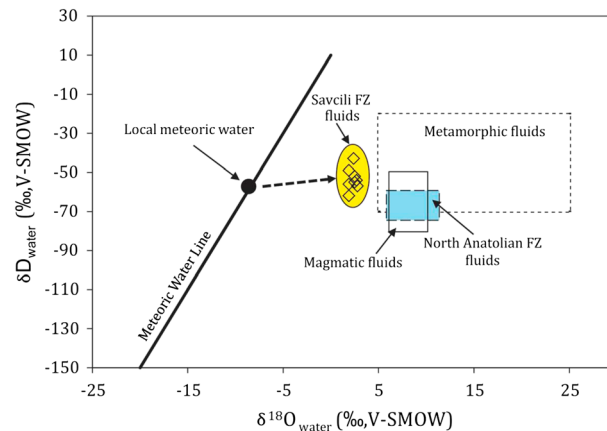ifferent size fractions consist of the same type of illite with crystallinity values characterized by illites forming under diagenetic conditions [*Verdel et al.*, 2012]. X-ray diffraction patterns indicate whole-rock powder samples, from which clays for Rb-Sr dating were separated, are free from feldspars, resulting from complete alteration to illite. Petrographic and mineralogic data clearly show that clay mineral assemblages from the fault rocks and their parent rocks are very different (Table 1). As the parent rocks do not contain authigenic illitic clay minerals, illite formation was restricted to the deformed fault rocks. This indicates that clay mineral authigenesis was not controlled by pervasive regional tectonic events but rather confined to areas of fluid circulation within the fault zone. This is an essential condition for unambiguous evaluation of the age dating of the Savcili Fault Zone.

9.2. Interpretation of Ar-Ar Ages

Different radioisotope dating methods were used on the same fault gouge minerals to provide reliable age constraints for the faulting episodes of the Savcili Fault Zone. Rb-Sr and Ar-Ar dating of the fault gouges gave discordant ages with the Ar-Ar dates being marginally older. It is recognized that K-Ar and Ar-Ar ages of mica minerals may be significantly older than the corresponding Rb-Sr ages due to the presence of excess [40]Ar in the mineral [e.g., *Li et al.*, 1994; *Inger et al.*, 1996; *de Jong et al.*, 2001; *Sherlock et al.*, 2008, and references therein]. Excess argon is particularly common in hydrothermal systems, shear zones, and metamorphic

Figure 13. Calculated δ^{18}O and δD values of fluids in equilibrium with illites from the Savcili fault gouges and their comparison those from the NAFZ.

environments [*Turner et al.*, 1993; *Vance et al.*, 1998; *Kelley*, 2002]. Excess ^{40}Ar is explained by either extra ^{40}Ar being incorporated into the crystal structure during crystallization from an Ar-rich fluid or by inheritance, as a result of incomplete recrystallization to release all Ar from relictic minerals [*de Jong et al.*, 2001]. However, complete homogenization of the Rb-Sr system, as discussed above, suggests strong fluid-assisted pervasive recrystallization making inherited ^{40}Ar unlikely. Slightly older Ar-Ar ages of the Savcili samples may rather be due to ^{40}Ar liberation into fluids through the dissolution of K-bearing detrital and diagenetic minerals during to tectonically controlled heat release and fluid flow [cf. *Sherlock et al.*, 2008]. Argon solubility is proportional to fluctuations in temperature. Therefore, as fluid temperatures decrease ^{40}Ar increasingly partitions into newly forming illite [*Kelley*, 2002].

9.3. Significance of the Illite Geochronology for Timing of the Savcili Fault Zone

There has been a controversy not only on the tectonic position of the SFZ and but also on its age. According to *Oktay* [1981] and *Seymen* [1982], the SFZ has been active until Quaternary. However, field observation is not consistent with such a young age of faulting, as the SFZ is cut by normal and oblique strike-slip faults that are overlaid by Neogene-Quaternary deposits. The isotopic dating of two fault rock samples (gouges) gathered from cataclastic zones offers better defined age constraints for the timing of faulting along the SFZ. Although Rb-Sr and Ar-Ar dating of the fault gouges yield somewhat discordant ages, the two different geochronological systems record the timing of two faulting events that occurred in the middle Eocene and late Oligocene-early Miocene. As discussed above, ages obtained from the Rb-Sr dating of the fault gouges reflect the timing of fault movements more closely. The isotopic ages provide evidence of major faulting during the Tertiary Alpine orogeny in central Turkey. The illite Rb-Sr age of sample *SAV-38* is 22.9 ± 1.3 Ma, which is 18 Ma younger than sample *SAV-41* (40.9 ± 1.5 Ma), suggests the episodic formation of imbricate thrusts within the SFZ. Although there were two main phases of compression along the SFZ, progressive shortening may still have taken place between the middle Eocene and late Oligocene to early Miocene, albeit with much less intensity of the stress and associated fluid flow events. Otherwise, the isotopic dating would not have provided clearly defined, distinctive ages but would rather have disturbed the isotopic systematics leading to a scatter of the Rb-Sr plots and irregular Ar-Ar age spectra.

9.4. Implication of Stable Isotope and Trace Element Data for the Origin and Evolution of Fluids During Faulting Episodes

δ^{18}O values of the Savcili fault gouge illites are a function of the oxygen isotope composition of fluids from which the clays precipitated, temperature and water-rock ratio. Oxygen isotope compositions of the Savcili illites are very similar with a narrow range of δ^{18}O values (Figure 11). This indicates that the clays in locations *SAV-38* and *SAV-41* were precipitated from fluids with similar oxygen isotope compositions at similar temperatures and water-rock ratios. The fluid δ^{18}O values can be calculated using mineral-water fractionation equations, provided that the temperature of the clay precipitation can be estimated. Clay mineral authigenesis during sediment burial and hydrothermal events is broadly controlled by temperature. Thus, the illite formation reaction can be used as a paleotemperature indicator. A temperature of ~200°C is estimated for the formation of discrete illite [*Pollastro*, 1993] in samples *SAV-38* and *SAV-41* and considering their illite crystallinity values (see above) [*Ji and Browne*, 2000]. Based on this temperature estimate, calculated oxygen isotope compositions of fluids range from 1.9‰ to 2.8‰ for the Savcili illites (Figure 13). These fluid compositions are consistent with δ^{18}O values of deep basin brines (formation water), which may result from interaction of surface derived fluids with ^{18}O-enriched rocks at high temperatures under deep burial or

hydrothermal conditions [*Clayton et al.*, 1966; *Sheppard*, 1986]. In contrast to the δ^{18}O values, formation waters show generally small enrichment in deuterium in relation to local meteoric water during water-rock interaction. This allows the estimation of the initial isotopic composition of meteoric fluids. Based on the estimated paleotemperature of clay formations, the calculated δD values of fluids in equilibrium with the illitic clays range from −43 to −62‰ (Figure 13). These δD values are similar to the isotopic composition of meteoric waters from the low- to middle-latitude setting of Turkey that has been prevailing since the Late Cretaceous [*Van der Voo*, 1993]. These δD values are entirely consistent with the isotopic composition of the local meteoric water of the study area near Ankara [*Dirican et al.*, 2005], which is positioned at a midlatitude (39.1500°N) and relatively high-altitude (~1015 m) area (Figure 13). δ^{18}O and δD values of fluids responsible for illite precipitation are distinctive from the fluids of the North Anatolian Fault Zone (NAFZ) (Figure 13). Stable isotope compositions of the latter indicate metamorphic and/or magmatic origin of fluids mobilized during the major fault movements, rather than evolved basinal fluids [*Uysal et al.*, 2006]. Fluids from the NAFZ were mobilized from deep sources, possibly in the ductile lower crust [cf. *Faulkner and Rutter*, 2001]. The significant difference in stable isotope compositions of illites from the Savcili Fault Zone with those from the NAFZ may be a result of the SFZ being formed and controlled by fluid flow in the upper crustal, whereas the latter is a plate boundary-related deep fault system cutting through the Earth's crust and extending into the lower crust [cf. *Kennedy et al.*, 1997]. Stable isotope compositions of the SFZ indicate a semiclosed hydrologic system and limited fluid flow through thrust faults of isotopically distinct, externally derived fluids [cf., *Ghisetti et al.*, 2001].

Trace element composition of the Savcili illitic clays also has implications for fluid origins. Trace element compositions and certain element ratios can be useful as tracers of basinal and hydrothermal fluid chemistry. Significantly high Th/Sc and La/Sc ratios and low La/Th and Cr/Th ratios compared to those of PAAS (Table 4) indicate precipitation of the clays from fluids enriched in incompatible elements that are characteristic of upper continental crust rocks. REE compositions of illites with pattern similar to PAAS as well as radiogenic initial ^{87}Sr/^{86}Sr values of ≥0.71 (Figure 9) are also consistent with involvement of fluids that equilibrated with crustal rocks in deep fault conduits. In summary, stable isotope data together with REE compositions of the illites indicate that waters of meteoric origin evolved into basin brines through interaction with ^{18}O-enriched rocks at high temperatures and under deep burial conditions. These fluids were mobilized during phases of compressional deformation and migrated upward along thrust faults toward shallow brittle deformation zones.

9.5. Tectonic Interpretation and Implications

The bottom part of the sedimentary cover overlying the crystalline basement in study area its surroundings consist of poorly sorted, coarse-grained (with block fragments) continental sediments, with detrital rock fragments originating mostly from the granitoid basement. Deposition of coarse-grained material was interpreted as a result of debris flow controlled by rapid uplift of sedimentary basin margins during faulting [*Whipple and Traylor*, 1996; *Gawthorpe and Leeder*, 2000]. A shear zone affecting the granitoid intrusion to the north of CACC has been related to an extensional event at 70 Ma [*Isik et al.*, 2008]. Similarly, transtensional tectonism has been reported in the region to the south of the SFZ, which occurred in association with a plutonic intrusion and controlled the formation of the Tuz Golu Basin [*Isik*, 2009]. *Lefebvre et al.* [2011, 2012] interpreted the exposure of the metamorphic rocks to the northwest of the SFZ as a result of rapid uplift due to an extensional regime. There is no direct depositional age data for the bottom part of the sedimentary units. A middle Paleocene-early Eocene age interval has been proposed by *Oktay* [1981] and *Goncuoglu et al.* [1994]. According to *Boztug et al.* [2009b], the intrusions in this region have been exposed at 58 Ma and provided detritus for the poorly sorted bottom section of the sedimentary units. Consequently, the depositional age of the continental units covering the crystalline basement is about late Paleocene. These continental sediments merge first into shallow marine containing Lutetian fossils and then deep marine sediments [*Oktay*, 1981].

Our Rb-Sr and Ar-Ar age data (~40 Ma and ~46 Ma, respectively) define a Lutetian age for faulting. This requires that the extensional regime that controlled the exposure of the basement rocks and the sedimentation of the Tertiary rocks terminated at ~40 Ma [cf. *Isik et al.*, 2008] with the start of compressional tectonics.
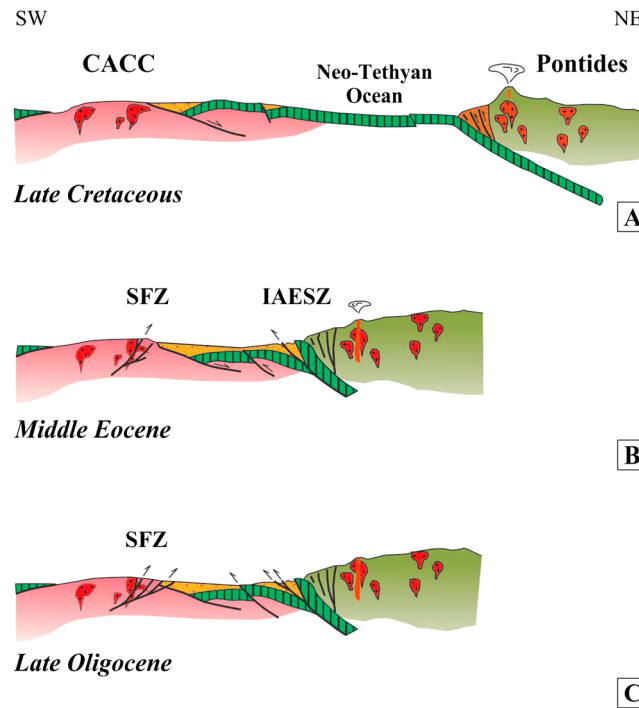
Figure 14. Schematic cross-sections illustrating the tectonic model for the exhumation of the CACC, followed by Paleocene to lower Eocene crustal extension and development of the SFZ during middle Eocene and late Oligocene.

Previous sedimentary records of continental subduction, high-pressure/low-temperature metamorphism, granite intrusions, obduction, and continent-continent collision in the Anatolide-Tauride Block, which are closely related, indicate that closure of Neo-Tethys and continental collision was probably initiated during the Palaeocene [*Okay et al.*, 2001, 2006; *Dangerfield et al.*, 2011]. However, the main deformation of the Anatolide-Tauride Block occurred in the middle Eocene and continued to the Miocene. The collision resulted in the large-scale south-vergent internal imbrication of the Anatolide-Tauride platform that produced the far-traveled nappe systems of the Taurides whereby the metamorphic axis of Anatolia was buried [*Sengor and Yılmaz*, 1981]. The SFZ represent these imbricate structures and our results show that a pulse of contractional activity following the closure of Neo-Tethys occurred around 40 Ma (Figure 14). This is consistent with previous estimates of timing for the main deformation, as mentioned above.

Crustal compression, folding, and thrusting continued with another main episode at ~ 23 Ma. We interpret our age data as thrusting that was mainly episodic in nature, resulting in complete resetting of isotopic systems with two distinct ages. This is also supported by different kinematic features of the older and younger faults, whereby the former resulted from a NE-SW oriented movement, while the latter represents a NNW-SSE movement (Figure 6).

We cannot recognize, with certainty, whether the contractional regime terminated at ~23 Ma or gradually diminished with weaker movement. Some constraints on the upper age limit of the thrusting are provided by field relationships of sedimentary records. In the study area and adjacent regions, Paleocene sediments are overlain unconformably by Neocene-Quaternary terrestrial sediments, with normal faults occurring along the basin margins. Neocene-Quaternary terrestrial sediments are widespread in central Turkey and commonly contain middle Miocene to Pliocene Mammal fossils [*Kara and Dönmez*, 1990; *Erdogan et al.*, 1996; *Kara*, 1991; *Karadenizli et al.*, 2005]. Consequently, the regional compression represented by the SFZ has been replaced by a period of regional extension.

The SFZ has previously been interpreted as a product of an extensional regime [*Genc and Yürür*, 2004; *Yurur and Genc*, 2006]. However, our field observations indicate (1) a lack of detachment faults in the area and (2) the occurrence of thrust/reverse faults along strike of the study area suggesting tectonism was dominated by a compressional regime.

As we demonstrated in this study, direct dating of brittle thrust faults significantly adds to the reconstruction of the regional geological history of the central Turkey, which previously relied on field relationships. Similar studies in future will provide further insight into the mechanics of thrust wedges and the evolution of the exhumed Tethyan orogenic belt not only in the Mediterranean region but also in the entire Alpine-Himalayan system. Finally, besides regional implications, direct dating of brittle faulting is a relatively new and exciting field in tectonics and offers a prolific approach for determining the absolute timing of tectonic events in areas that have largely relied on indirect information. Direct dating of brittle faulting offers a unique and novel

approach to better understand paleoseismicity, and particularly, when combined with stable isotope work, new insights in not only the origin and evolution of tectonically mobilized fluids but also the development of paleotopography for young and actively deforming orogens [*Chamberlain and Poage*, 2000; *Charreau et al.*, 2012].

10. Conclusion

A combination of field observations, microstructure, and isotopic studies of fault gouges allows reconstruction of the tectonic evolution of central Turkey. This provides new insight into the complex tectonic history of the eastern Mediterranean region. The following conclusions can be drawn from these studies:

1. The SFZ has evolved through a series of faulting events with well-developed cataclastic zones consisting of well-defined fault core and a damage zone. These cataclastic zones are characterized by pervasive fracturing, cataclasites, gouges and clast- or matrix-supported breccias, and fault surface(s).
2. The SFZ developed under compressional tectonic regime with a NE-SW horizontal direction of principal stress.
3. The SFZ consists of anastomosing reverse/thrust faults with WNW-ESE direction that placed rocks of the Central Anatolian Crystalline Complex on Paleogene sedimentary units. Structural measurements on slickensides and kinematic indicators (V or crescentic markings, steps, fractures, and trailed materials) show that faults within the SFZ have top to the NE and NW sense of brittle deformation sharing.
4. Stable isotope (δ^{18}O and δ D) and trace element compositions of fault gouge illites indicate that deep basinal brines (formation water) were mobilized during phases of compressional deformation. These fluids migrated along thrust faults toward shallow brittle deformation zones where illite precipitated.
5. We used different radioisotope dating methods, Rb-Sr and Ar-Ar, on the same fault gouge minerals from two cataclastic zones to provide reliable age constraints for the faulting episodes of the Savcili Fault Zone. Two different dating techniques demonstrate age variability, with ages of 40.9 ± 1.5 Ma and 22.9 ± 1.3 Ma obtained by Rb-Sr dating, whereas Ar-Ar technique provided ages of 46.45 ± 0.25 Ma and 29.8 ± 0.13 Ma. We propose that marginally older Ar-Ar dates are due to excess ^{40}Ar, and thus, Rb-Sr dating provides ages more closely reflecting the timing of fault movements.
6. Reactivation of the SFZ occurred during at least two phases; the middle Eocene and late Oligocene to early Miocene, which is consistent with the relative age constraints suggested by field relationships.
7. The SFZ represents a rapid change in the stress regime from extension to contraction at ~40 Ma.
8. Direct dating of brittle faulting provides a prolific approach for determining the absolute timing of tectonic events in areas that have largely relied on indirect information.

References

Allmendinger, R. W. (2001), FaultKinWin, a program for analyzing fault slip data for Windows™ computers, Version 1.1.

Alpaslan, M., R. Frei, D. Boztug, M. A. Kurt, and A. Temel (2004), Geochemical and Pb-Sr-Nd isotopic constraints indicating an enriched-mantle source for Late Cretaceous to early Tertiary volcanism, Central Anatolia, Turkey, *Int. Geol. Rev.*, *46*, 1022–1041.

Alpaslan, M., D. Boztug, R. Frei, A. Temel, and M. A. Kurt (2006), Geochemical and Pb–Sr–Nd isotopic composition of the ultrapotassic volcanic rocks from the extension-related Camardi-Ulukisla basin, Nigde Province, Central Anatolia, Turkey, *J. Asian Earth Sci.*, *27*, 613–627.

Angelier, J. (1984), Tectonic analysis of fault-slip data sets, *J. Geophys. Res.*, *89*, 5835–5848, doi:10.1029/JB089iB07p05835.

Ataman, G. (1972), Ankara'nın güneydoğusundaki granitik/granodiyoritik kütlelerden Cefalıkdağı radyometrik yaşı hakkında ön çalışma, *H.Ü Fen ve Mühendislik Bilimleri Derg.*, *2*(1), 44–49.

Ayan, M. (1963), Contribution a l'etude petrographique et ge'ologigue de la region situêau Nord-Est de Kaman (Turquie), *MTA*, *115*, 332.

Boztug, D. (2000), S-I-A type intrusive associations: Geodynamic significance of synchronism between metamorphism and magmatism in central Anatolia, Turkey, in *Tectonics and Magmatism in Turkey and the Surrounding Area*, edited by E. Bozkurt, J. Winchester, and J. A. Piper, *Geol. Soc. London Spec. Publ.*, *173*, 407–424.

Boztug, D., and R. C. Jonckheere (2007), Apatite fission-track data from central Anatolian granitoids (Turkey) constrain Neo-Tethyan closure, *Tectonics*, *26*, TC3011, doi:10.1029/2006TC001988.

Boztug, D., O. Güney, M. Heizler, R. C. Jonckheere, M. Tichomirowa, and N. Otlu (2009a), 207Pb-206Pb, 40Ar-39Ar and fission-track geothermochronology quantifying cooling and exhumation history of the Kaman-Kırşehir region ıntrusions, central Anatolia, Turkey, *Turk. J. Earth Sci.*, *18*, 85–108.

Boztug, D., R. C. Jonckheere, M. Heizler, L. Ratschbacher, Y. Harlavan, and M. Tichomirova (2009b), Timing of post-obduction granitoids from intrusion through cooling to exhumation in central Anatolia, Turkey, *Tectonophysics*, *473*(1–2), 223–233.

Caglayan, A. (2010), Structural analysis of the Savcili Fault Zone, Kirsehir, MS thesis, 82 pp., Ankara Univ., Graduate School of Natural and Applied Science, Dep. of Geological Engineering, Ankara, Turkey.

Capan, U. Z., and P. A. Floyd (1985), Geochemical and petrogenetic features of metabasalts within units of the Ankara mélange, Turkey, *Ofioliti*, *10*, 3–18.

Cemen, I., M. C. Goncuoglu, and K. Dirik (1999), Structural evolution of the Tuzgölü Basin in central Anatolia, Turkey, *J. Geol.*, *107*, 693–706.

Chamberlain, C. P., and M. A. Poage (2000), Reconstructing the paleotopography of mountain belts from the isotopic composition of authigenic minerals, *Geology*, *28*, 115–118.

Charreau, J., M. L. Kent-Corson, L. Barrier, R. Augier, B. D. Ritts, Y. Chen, C. FranceLannord, and C. Guilmette (2012), A high-resolution stable isotopic record from the Junggar Basin (NW China): Implications for the paleotopographic evolution of the Tianshan Mountains, *Earth Planet. Sci. Lett.*, *341/344*, 158–169.

Clark, M., and A. H. F. Robertson (2002), The role of the Early Tertiary Ulukısla Basin, southern Turkey, in suturing of the Mesozoic Tethys ocean, *J. Geol. Soc. London*, *159*, 673–690.

Clark, M., and A. H. F. Robertson (2005), Uppermost Cretaceous-Lower Tertiary Ulukisla Basin, south-central Turkey: Sedimentary evolution of part of a unified basin complex within an evolving Neotethyan suture zone, *Sediment. Geol.*, *173*, 15–51.

Clauer, N., S. Chaudhuri, S. Kralik, and C. Bonnotcourtois (1993), Effects of experimental leaching on Rb-Sr and K-Ar isotopic systems and REE contents of diagenetic illite, *Chem. Geol.*, *103*(1-4), 1–16.

Clayton, R. N., I. Friedman, D. L. Graf, T. K. Mayeda, W. F. Meents, and N. F. Shimp (1966), The origin of saline formation waters, *J. Geophys. Res.*, *71*, 3869–3882, doi:10.1029/JZ071i016p03869.

Dangerfield, A., R. Harris, E. Sarifakioglu, and Y. Dilek (2011), Tectonic evolution of the Ankara Mélange and associated Eldivan ophiolite near Hançili, central Turkey, *Geol Soc. Am. Spec. Pap.*, *480*, 143–169.

de Jong, K., G. Féraud, G. Ruffet, M. Amouric, and J. R. Wijbrans (2001), Excess argon incorporation in phengite of the Mulhacén Complex: Submicroscopic illitization and fluid ingress during late Miocene extension in the Betic Zone, south-eastern Spain, *Chem. Geol.*, *178*, 159–195.

Delvaux, D., and B. Sperner (2003), Stress tensor inversion from fault kinematic indicators and focal mechanism data: The TENSOR program, in *New Insights Into Structural Interpretation and Modelling*, edited by D. Nieuwland, *Geol. Soc. London Spec. Publ.*, *212*, 75–100.

Derman, A. S., B. Rojay, H. Güney, and M. Yildiz (2000), New sedimentological data on the evolution of Sereflikochisar-Aksaray fault zone, in *Haymana-Tuzgolu-Ulukisla Basins Workshop*, *TAPG Spec. Publ.*, vol. 5, pp. 47–70, Aksaray, Turkey.

Diran, A., S. Unal, Y. Acar, and M. Demircan (2005), The temporal and seasonal variation of H-2 and O-18 in atmospheric water vapour and precipitation from Ankara, Turkey in relation to air mass trajectories at the Mediterranean Basin, in *Isotopic Composition of Precipitation in the Mediterranean Basin in Relation to Air Circulation Patterns and Climate*, pp. 191–214, IAEA, Vienna.

Dirik, K., and M. C. Goncuoglu (1996), Neotectonic characteristics of central Anatolia, *Int. Geol. Rev.*, *38*, 807–817.

Doblas, M. (1998), Slickenside kinematic indicators, *Tectonophysics*, *295*, 187–197.

Dong, H., C. M. Hall, D. R. Peacor, and A. N. Halliday (1995), Mechanisms of argon retention in clays revealed by laser ^{40}Ar/^{39}Ar dating, *Science*, *267*, 355–359.

Duvall, A. R., K. C. Marin, B. A. van der Pluijm, and L. Chuanyou (2011), Direct dating of Eocene reverse faulting in northeastern Tibet using Ar-dating of fault clays and low-temperature thermochronometry, *Earth Planet. Sci. Lett.*, *304*, 520–526.

Eggins, S. M., J. D. Woodhead, L. P. J. Kinsley, G. E. Mortimer, P. Sylvester, M. T. McCulloch, J. M. Hergt, and M. R. Handler (1997), A simple method for the precise determination of $>$=40 trace elements in geological samples by ICPMS using enriched isotope internal standardisation, *Chem. Geol.*, *134*, 311–326.

Erdogan, B., E. Akay, and S. M. Ugur (1996), Geology of the Yozgat region and evolution of the collisional Cankırı basin, *Int. Geol. Rev.*, *38*, 788–806.

Faccenna, C., O. Bellier, J. Martinod, C. Piromallo, and V. Regard (2006), Slab detachment beneath eastern Anatolia: A possible cause for the formation of the North Anatolian fault, *Earth Planet. Sci. Lett.*, *242*, 85–97.

Faulkner, D. R., and E. H. Rutter (2001), Can the maintenance of overpressured fluids in large strike-slip fault zones explain their apparent weakness?, *Geology*, *29*(6), 503–506.

Gawthorpe, R. L., and M. R. Leeder (2000), Tectono-sedimentary evolution of active extensional basins, *Basin Res.*, *12*, 195–218.

Genc, Y., and M. T. Yürür (2010), Coeval extension and compression in Late Mesozoic-Recent thin-skinned extensional tectonics in central Anatolia, Turkey, *J. Struct. Geol.*, *32*, 623–640.

Genc, Y., and T. Yürür (2004), The Kirsehir detachment faulting and a new interpretation of the "Savcili Trust Zone" in central Anatolia, Turkey, in *Proceedings 5th International Symposium on Eastern Mediterranean Geology, Thessalloniki, Greece*, vol. 1, edited by A. A. Chatzipetros and S. B. Pavlides, pp. 73–76, Thessalloniki, Greece.

Ghisetti, F., D. L. Kirschner, L. Vezzani, and F. Agosta (2001), Stable isotope evidence for contrasting paleofluid circulation in thrust faults and normal faults of the central Apennines, Italy, *J. Geophys. Res.*, *106*, 8811–8825.

Goncuoglu, M. C. (2009), Comment on "207Pb–206Pb single-zircon evaporation ages of some granitoid rocks reveal continent-oceanic island arc collision during the Cretaceous geodynamic evolution of the central Anatolian crust, Turkey"—Boztug, D., M. Tichomirowa, and K. Bombach 2007, 31, 71–86, 2009, *J. Asian Earth Sci.*, *34*, 796–797.

Goncuoglu, M. C., V. Toprak, I. Kuscu, A. Erler, and E. Olgun (1991), Orta Anadolu Masifi'nin batı bölümünün jeolojisi, Bölüm 1: Güney Kesim. TPAO Rap., No. 2909,140.

Goncuoglu, M. C., A. Erler, V. Toprak, E. Olgun, K. Yaliniz, I. Kuscu, S. Koksal, and K. ve Dirik (1993), Orta Anadolu Masifinin Orta Bölümünün Jeolojisi, Bölüm 3: Orta Kızılırmak Tersiyer Baseninin Jeolojik Evrimi, TPAO Rapor No: 3313, 104.

Goncuoglu, M. C., A. Erler, K. Dirik, and K. Yaliniz (1994), Sivas Baseni'nin Batısı'nın Jeolojisi, 1993 Saha Raporu, ODTÜ AGÜDOS Proje No: 93-03-09-01-06, 8.

Gorur, N., F. Y. Oktay, I. Seymen, and A. M. C. Sengor (1984), Palaeotectonic evolution of the Tuzgolu Basin complex, central Turkey: Sedimentary record of a Neotethyan closure, in *The Geological Evolution of the Eastern Mediterranean*, edited by J. E. Dixon and A. H. F. Robertson, *Geol. Soc. London Spec. Publ., 17*, 467–482.

Gorur, N., O. Tüysüz, and A. M. C. Sengör (1998), Tectonic evolution of the Central Anatolian Basins, *Int. Geol. Rev.*, *40*, 831–850.

Gursoy, H., J. D. A. Piper, O. Tatar, and H. Temiz (1997), A paleomagnetic study of the Sivas basin, Central Turkey: Crustal deformation during lateral extrusion of the Anatolian block, *Tectonophysics*, *271*, 89–105.

Gursoy, H., J. D. A. Piper, O. Tatar, and L. Mesci (1998), Paleomagnetic study of the Karaman and Karapinar volcanic complexes, central Turkey: Neotectonic rotation in the south-central sector of the Anatolian block, *Tectonophysics*, *299*, 191–211.

Haines, S. H., and B. A. van der Pluijm (2008), Clay quantification and Ar-Ar dating of synthetic and natural gouge: Application to the Miocene Sierra Mazatan detachment fault, Sonora, Mexico, *J. Struct. Geol.*, *30*(4), 525–538.

Hall, C. M. (2013), Direct measurement of recoil effects on ^{40}Ar/^{39}Ar standards, in *Advances in ^{40}Ar/^{39}Ar Dating: From Archaeology to Planetary Sciences*, edited by F. Jourdan, D. F. Mark, and C. Verati, *Geol. Soc. London Spec. Publ.*, 53–62.

Hall, C. M., P. L. Higueras, S. E. Kesler, R. Lunar, H. Dong, and A. N. Halliday (1997), Dating of alteration episodes related to mercury mineralization in the Almadén district, Spain, *Earth Planet. Sci. Lett.*, *148*, 287–298.

Hancock, P. L. (1985), Brittle microtectonics: Principles and practice, *J. Struct. Geol.*, *7*, 437–457.

Hetzel, R., H. Zwingmann, A. Mulch, K. Gessner, C. Akal, A. Hampel, T. Güngör, R. Petschick, T. Mikes, and F. Wedin (2013), Spatiotemporal evolution of brittle normal faulting and fluid infiltration in detachment fault systems: A case study from the Menderes Massif, western Turkey, *Tectonics*, *32*, 364–376, doi:10.1002/tect.20031.

Ilbeyli, N., J. A. Pearce, M. F. Thirwall, and J. G. Mitchell (2004), Petrogenesis of collision-related plutonics in central Anatolia, Turkey, *Lithos*, *72*, 163–182.

Inger, S., W. Ramsbottom, R. A. Cliff, and D. C. Rex (1996), Metamorphic evolution of the Sesia-Lanzo Zone, Western Alps: Time constraints from multi-system geochronology, *Contrib. Mineral. Petrol.*, *126*, 152–168.

Isik, V. (2009), The ductile shear zone in granitoid of the Central Anatolian Crystalline Complex, Turkey: Implications for the origins of the Tuzgölü basin during the Late Cretaceous extensional deformation, *J. Asian Earth Sci.*, *34*, 507–521.

Isik, V., C. H. Lo, C. Goncuoglu, and S. Demirel (2008), ^{39}Ar/^{40}Ar ages from the Yozgat Batholith: Preliminary data on the timing of Late Cretaceous extension in the Central Anatolian Crystalline Complex, Turkey, *J. Geol.*, *116*(5), 510–526.

Isik, V., A. Caglayan, G. Seyitoglu, T. Uysal, J. Zhao, K. Sozeri, and K. Esat (2010a), Geology of the Savcılı Fault Zone, central Turkey, Tectonic Crossroads: Evolving orogens of Eurasia-Africa-Arabia, Abstracts with Programs, (8-2), 32, Geol. Soc. of Am., Ankara, Turkey.

Isik, V., G. Seyitoglu, A. Caglayan, T. Uysal, J. Zhao, K. Sozeri, and K. Esat (2010b), Cataclastic Zone within the Savcılı Fault Zone, central Turkey, Abstract T51A-2011 presented at 2010 Fall Meeting, AGU, San Francisco, Calif., 13–17 Dec.

Isik, V., A. Caglayan, T. Uysal, and R. Bolhar (2011), Microstructures of the Kirsehir Complex, central Turkey, Abstract T43C-2337 presented at 2011 Fall Meeting, AGU, San Francisco, Calif., 5–9 Dec.

Jaffey, N., and A. Robertson (2005), Non-marine sedimentation associated with Oligocene—Recent exhumation and uplift of the central Taurus Mountains, S Turkey, *Sediment. Geol.*, *73*, 53–89.

Ji, J., and P. R. L. Browne (2000), Relationship between illite crystallinity and temperature in active geothermal systems of New Zealand, *Clays Clay Miner.*, *48*, 139–144.

Kadioglu, Y. K., Y. Dilek, N. Gulec, and K. A. Foland (2003), Tectonomagmatic evolution of bimodal plutons in the Central Anatolian Crystalline Complex, Turkey, *Geol. J.*, *111*, 671–690.

Kara, H. (1991), 1/100.000 ölçekli Türkiye Jeoloji haritası, Kırşehir-G18 paftası ve açıklaması, MTA Enst. Yayınl. No. 37, 12.

Kara, H., and M. Dönmez (1990), 1/100.000 ölçekli Türkiye Jeoloji haritası, Kırşehir-G17 paftası ve açıklaması, MTA Enst. Yayınl. No. 34, 17.

Karadenizli, L., G. Seyitoglu, S. Sen, N. Arnaud, N. Kazancı, G. Sarac, and C. Alcicek (2005), Mammal bearing late Miocene tuffs of the Akkasdagi region: Distribution, age, petrographical and geochemical characteristics, *Geodiversitas*, *27*(4), 553–566.

Kelley, S. (2002), Excess argon in K–Ar and Ar–Ar geochronology, *Chem. Geol.*, *188*, 1–22.

Kennedy, B. M., Y. K. Kharaka, W. C. Evans, A. Ellwood, D. J. DePaolo, J. Thordsen, G. Ambats, and R. H. Mariner (1997), Mantle fluids in the San Andreas fault system, California, *Science*, *278*, 1278–1281.

Kissel, C., C. Laj, A. Poisson, and N. Gorur (2003), Paleomagnetic reconstruction of the Cenozoic evolution of the eastern Mediterranean, *Tectonophysics*, *362*, 199–217.

Kocyigit, A. (1991), An example of an accretionary forearc basin from northern Central Anatolia and its implications for the history of subduction of Neo-Tethys in Turkey, *Geol. Soc. Am. Bull.*, *103*, 22–36.

Kocyigit, A. (2003), Orta Anadolu'nun genel Neotektonik Özellikleri ve Depremselliği. Haymana-Tuzgölü-Ulukışla Basenleri Uygulamalı Çalışma, *TPJD*, (Özel sayı:5), 1–26.

Kocyigit, A., and A. Beyhan (1998), A new intracontinental transcurrent structure: The Central Anatolian Fault Zone, Turkey, *Tectonophysics*, *284*, 317–336.

Koksal, S., R. L. Romer, M. C. Goncuoglu, and F. Toksoy-Koksal (2004), Timing of post-collision H-type to A-type granitic magmatism: U-Pb titanite ages from the Alpine central Anatolian granitoids Turkey, *Int. J. Earth Sci.*, *93*, 974–989.

Lefebvre, C., A. Barnhoorn, D. J. J. van Hinsbergen, N. Kaymakci, and R. L. M. Vissers (2011), Late Cretaceous extensional denudation along a marble detachment fault zone in the Kırşehir massif near Kaman, central Turkey, *J. Struct. Geol.*, *33*, 1220–1236.

Lefebvre, C., A. Barnhoorn, D. J. J. van Hinsbergen, N. Kaymakci, and R. L. M. Vissers (2012), Reply to Genç and Yürür's comments on: "Late Cretaceous extensional denudation along a marble detachment fault zone in the Kırşehir massif near Kaman, Central Turkey", *J. Struct. Geol.*, *36*, 90–93.

Lefebvre, C., M. J. M. Meijers, N. Kaymakci, A. Peynircioglu, C. G. Langereis, and D. J. J. van Hinsbergen (2013), Reconstructing the geometry of central Anatolia during the late Cretaceous: Large-scale Cenozoic rotations and deformation between the Pontides and Taurides, *Earth Planet. Sci. Lett.*, *366*, 83–98.

Li, S., S. Wang, Y. Chen, D. Liu, J. Qiu, H. Zhou, and Z. Zhang (1994), Excess argon in phengite from eclogite: Evidence from dating of eclogite minerals by Sm–Nd, Rb–Sr and ^{40}Ar/^{39}Ar methods, *Chem. Geol.*, *112*, 343–350.

Ludwig, K. R. (2003), *User's Manual for Isoplot 3.00. A Geochronological Toolkit for Microsoft Excel*, Special Publication, 4a, Berkeley Geochronology Center, Berkeley, Calif.

Merrriman, R. J., and M. Frey (1999), Patterns of very low-grade metamorphism in metapelitic rocks, in *Low Grade Metamorphism*, edited by M. Frey and D. Robinson, pp. 61–107, Blackwell Science, Cambridge.

Moix, P., L. Beccaletto, H. W. Kozur, C. Hochard, F. Rosselet, and G. M. Stampfli (2008), A new classification of the Turkish terranes and sutures and its implication for the paleotectonic history of the region, *Tectonophysics*, *451*, 7–39.

Moore, D. M., and R. C. Reynolds (1997), *X-ray Diffraction and the Identification and Analysis of Clay Minerals*, 378 pp., Oxford Univ. Press, Oxford.

Mutlu, H., I. T. Uysal, E. Altunel, V. Karabacak, Y. Feng, J. Zhao, and O. Atalay (2010), Rb–Sr systematics of fault gouges from the North Anatolian Fault Zone (Turkey), *J. Struct. Geol.*, *32*, 216–221.

Okay, A. I., and O. Tüysüz (1999), Tethyan sutures of northern Turkey, in *The Mediterranean Basins: Tertiary Extension Within the Alpine Orogen*, edited by B. Durand et al., *Geol. Soc. London Spec. Publ.*, 475–515.

Okay, A. I., I. Tansel, and O. Tüysüz (2001), Obduction, subduction and collision as reflected in the Upper Cretaceous-Lower Eocene sedimentary record of western Turkey, *Geol. Mag.*, *138*(2), 117–142.

Okay, A. I., O. Tüysüz, M. Satır, S. Ozkan-Altıner, D. Altıner, S. Sherlock, and R. H. Eren (2006), Cretaceous and Triassic subduction-accretion, high-pressure-low-temperature metamorphism, and continental growth in the Central Pontides, Turkey, *Geol. Soc. Am. Bull.*, *118*(9), 1247–1269.

Oktay, F. Y. (1981), Savcılıbüyükoba (Kaman) çevresinde Orta Anadolu Masifi tortul örtüsünün jeolojisi ve sedimantolojisi, Doçentlik Tezi, 175 pp., İ.T.Ü. Maden Fakültesi, İstanbul.

Orife, T., and R. J. Lisle (2003), Numerical processing of paleostress results, *J. Struct. Geol.*, *25*, 949–957.

Platzman, E. S., C. Tapirdamaz, and M. Sanver (1998), Neogene anticlockwise rotation of central Anatolia (Turkey): Preliminary paleomagnetic and geochronological results, *Tectonophysics*, *299*, 175–189.

Poisson, A., J. C. Guezou, A. Ozturk, S. Inan, H. Temiz, H. Gursoy, K. S. Kavak, and S. Ozden (1996), Tectonic setting and evolution of the Sivas basin, *Int. Geol. Rev.*, *38*, 833–853.

Pollastro, R. M. (1993), Considerations and applications of the illite/smectite geothermometer in hydrocarbon-bearing rocks of Miocene to Mississippian age, *Clays Clay Miner.*, *41*, 119–133.

Robertson, A. H. F., and J. E. Dixon (1984), Introduction: aspects of the geological evolution of the eastern Mediterranean, in *The Geological Evolution of the Eastern Mediterranean*, edited by J. E. Dixon and A. H. F. Robertson, *Geol. Soc. London Spec. Publ., 17*, 1–74.

Samson, S. D., and E. C. J. Alexander (1987), Calibration of the interlaboratory ^{40}Ar/^{39}Ar dating standard, MMhb-1, *Chem. Geol. Isot. Geosci.*, *66*, 27–34.

Sengor, A. M. C., and B. A. Natalin (1996), Paleotectonics of Asia: Fragment of a synthesis, in *The Tectonics of Asia*, edited by A. Yin and T. M. Harrison, pp. 486–640, Cambridge Univ. Press, New York.

Sengor, A. M. C., and Y. Yılmaz (1981), Tethyan evolution of Turkey: A plate tectonic approach, *Tectonophysics*, *75*, 181–241.

Sengor, A. M. C., N. Gorur, and F. Saroglu (1985), Strike-slip faulting and related basin formation in zones of tectonic escape: Turkey as a case study, in *Strike-Slip Deformation, Basin Formation and Sedimentation*, *Spec. Publ.*, vol. 37, edited by K. T. Biddle and N. Christie Blick, pp. 227–264, Soc. Eco. Palaeo. Mineral, Tulsa, Okla.

Seymen, I. (1982), Kaman dolayında Kırşehir Masifinin jeolojisi, Doktora Tezi, 164 pp., İTÜ Maden Fakültesi.

Seymen, I. (1984), Kırşehir masifi metamorfitlerinin jeoloji evrimi, in *Ketin Sempozyumu*, pp. 133–148, Türkiye Jeoloji Kurumu Yayını, Ankara.

Sharp, Z. D. (1990), Laser-based microanalytical method for the in situ determination of oxygen isotope ratios of silicates and oxides, *Geochim. Cosmochim. Acta*, *54*, 1353–1357.

Sheppard, S. M. F. (1986), Characterization and isotopic variations in natural waters, in *Stable Isotopes in High Temperature Geological Processes*, *Rev. in Miner.*, vol. 16, edited by J. W. Valley, H. P. Taylor Jr., and J. R. O'Neil, pp. 165–183, Washington, D. C.

Sherlock, S. C., J. Zalasiewicz, S. P. Kelley, and J. Evans (2008), Excess 40Ar uptake during slate formation: A ^{40}Ar/^{39}Ar UV laserprobe study of muscovite strain-fringes from the Palaeozoic Welsh Basin, UK, *Chem. Geol.*, *257*, 206–220.

Srodon, J., and D. D. Eberl (1984), Illite, in *Reviews in Mineralogy*, vol. 13, edited by W. Bailey, pp. 495–544, Mineralog. Soc. of Am., Washington, D. C.

Tatar, O., J. D. A. Piper, H. Gursoy, and H. Temiz (1996), Palaeomagnetic significance of neotectonic counterclockwise rotation in central Turkey, *Int. Geol. Rev.*, *38*, 692–700.

Taylor, S. R., and S. M. McLennan (1985), *The Continental Crust: Its Composition and Evolution*, Blackwell, 312 pp., Oxford, U. K.

Turner, G., P. Burnard, J. L. Ford, J. D. Gilmour, I. C. Lyon, and F. M. Stuart (1993), Tracing fluid sources and interactions, *Philos. Trans. R. Soc. London A*, *344*, 127–140.

Uysal, I. T., H. Mutlu, E. Altunel, V. Karabacak, and S. D. Golding (2006), Clay mineralogical and isotopic (K–Ar, dO-18, dD) constraints on the evolution of the North Anatolian fault zone, Turkey, *Earth Planet. Sci. Lett.*, *243*(1–2), 181–194.

Uysal, I. T., Y. X. Feng, J. X. Zhao, R. Bolhar, V. Isik, K. Baublys, A. Yago, and S. D. Golding (2011), Seismic cycles recorded in late Quaternary calcite veins: Geochronological, geochemical and microstructural evidence, *Earth Planet. Sci. Lett.*, *303*, 84–96.

Vance, D., M. Ayres, S. P. Kelley, and N. B. W. Harris (1998), The thermal response of a metamorphic belt to extension: Constraints from laser Ar data on metamorphic micas, *Earth Planet. Sci. Lett.*, *162*, 153–164.

van der Pluijm, B. A., C. M. Hall, P. J. Vrolijk, D. R. Pevear, and M. C. Covey (2001), The dating of shallow faults in the Earth's crust, *Nature*, *412*, 172–175.

van der Pluijm, B. A., P. J. Vrolijk, D. R. Pevear, C. M. Hall, and J. Solum (2006), Fault dating in the Canadian Rocky Mountains: Evidence for late cretaceous and early Eocene orogenic pulses, *Geology*, *34*(10), 837–840.

Van der Voo, R. (1993), *Paleomagnetism of the Atlantic, Tethys and Iapetus Oceans*, 405 pp., Cambridge Univ. Press, Cambridge, U. K.

Verdel, C., B. A. van der Pluijm, and N. Niemi (2012), Variation of illite/muscovite ^{40}Ar/^{39}Ar spectra during progressive low-grade metamorphism: An example from the US Cordillera, *Contrib. Mineral. Petrol.*, *164*, 521–536.

Whipple, K. X., and C. R. Traylor (1996), Tectonic control on fan size: The importance of spatially-variable subsidence rates, *Basin Res.*, *8*, 351–366.

Whitney, D. L., and M. A. Hamilton (2004), Timing of high grade metamorphism in central Turkey and the assembly of Anatolia, *J. Geol. Soc. London*, *161*, 823–828.

Whitney, D. L., C. Teyssier, A. K. Fayon, M. A. Hamilton, and M. J. Heizler (2003), Tectonic controls on metamorphism, partial melting, and intrusion: Timing of regional metamorphism and magmatism of the Nigde Massif, Turkey, *Tectonophysics*, *376*, 37–60.

Yaliniz, M. K., and M. C. Goncuoglu (1996), Suprasubduction zone ophiolites of Central Anatolia: Geochemical evidence from the Sarıkaman ophiolite, Aksaray, Turkey, *Mineral. Mag.*, *60*, 697–710.

Yaliniz, M. K., N. S. Aydın, M. C. Goncuoglu, and O. Parlak (1999), Terlemez quartz monzonite of central Anatolia (Aksaray-Sarıkaraman): Age, petrogenesis and geotectonic implications for ophiolite emplacement, *Geol. J.*, *34*, 233–242.

Yaliniz, M. K., M. C. Goncuoglu, and S. Ozkan-Altiner (2000), Formation and emplacement ages of the SSZ-type Neotethyan ophiolites in central Anatolia, Turkey: Palaeotectonic implications, *Geol. J.*, *35*(2), 53–68.

Yamasaki, S., H. Zwingmann, K. Yamada, T. Tagami, and K. Umeda (2013), Constraining the timing of brittle deformation and faulting in the Toki granite, central Japan, *Chem. Geol.*, *351*, 168–174.

Yurur, M. T., and Y. Genc (2006), The Savcılı Thrust Fault (Kırşehir, Central Anatolia): A backthrust fault, a suture zone or secondary fracture in extensional regime?, *Geol. Carpathica*, *57*, 47–56.

Zwingmann, H., R. Han, and J. H. Ree (2011), Cretaceous reactivation of the Deokpori Thrust, Taebaeksan Basin, South Korea, constrained by K-Ar dating of clayey fault gouge, *Tectonics*, *30*, TC5015, doi:10.1029/2010TC002829.